IDŐJÁRÁS

CONTENTS

****

http://omsz.met.hu/english/ref/jurido/jurido_en.html

Estimating soil moisture content of a grass-covered surface using an energy balance approach and agroclimatological observations

Ferenc Ács[1*], **Gábor Szász**[2] and **Miklós Drucza**[1]

[1]*Eötvös Loránd University, Department of Meteorology,*
P.O. Box 32, H-1518 Budapest, Hungary

[2]*University of Debrecen, P.O. Box 36, H-4015 Debrecen, Hungary*

Abstract—Diagnostic applications of the energy balance equation for vegetated surface (VSEBE) are briefly summarized. We tested whether VSEBE can be successfully applied for estimating surface soil moisture content (θ) in the growing season using agroclimatological observations. The analysis is performed using data set of the Agrometeorological Observatory of the University of Debrecen collected in the period 1974–1986.

In the study, the process-based VSEBE model is described in detail. It is shown that VSEBE is not suitable for estimating instantaneous values of θ, since the applicability of the model is fairly limited and the scattering of the estimates is relatively large. It is also shown that monthly mean values of θ can be estimated with acceptable accuracy applying VSEBE for a long time period. The results obtained can be useful for estimating climate characteristics of agrometeorological stations.

Key-words: agrometeorological station, grass-covered surface, energy balance equation, surface soil moisture content surface soil moisture content, instantaneous value of surface soil moisture content, monthly mean value of surface soil moisture content.

1. Introduction

The energy balance equation above vegetated surface is the basic equation for quantifying energy transfer processes at the land-surface/atmosphere interface. VSEBE can be applied either in prognostic or diagnostic mode. In both applications, the ground surface temperature T_g (for details see Section 3), and

---

* Corresponding author; E-mail: acs@caesar.elte.hu

the soil surface moisture content θ are intrinsically coupled. In this study, the attention is paid to diagnostic applications. The diagnostic application of VSEBE depends on the availability of T_g and θ (*Table 1*). When both T_g and θ are available, the Penman-Monteith's equation can be used to calculate the latent heat flux *LE*. Net radiation R_n can be simply estimated using radiation balance equation RBE; surface soil heat flux G can be parameterized either via R_n or using the force-restore method (*Bhumralkar*, 1975; *Ács et al.*, 2000), while sensible heat flux H is obtained as residual term of VSEBE (application 1) (*Ács et al.*, 2000). Note that deep soil temperature used in the force-restore method can be expressed via T_g (*Ács et al.*, 1991). If T_g is not directly available, R_n can be given (*Holtslag* and *van Ulden*, 1983). When θ is available but T_g is unknown, this is referred to as application 2. In this case, T_g can be simply calculated from VSEBE (*van de Griend et al.*, 1985).

Table 1. The energy balance equation applications

Surface state variables	Applications			
	Parameterization of the fluxes			
	R_n	G	H	LE
Application 1				
Known θ and known T_g	Radiation balance equation	Per cent of R_n	Residual term	Penman-Monteith equation
Application 2				
Known θ and unknown T_g	Radiation balance equation	Fourier equation, Force-restore method	Bulk formula	Bulk formula
Application 3				
Unknown θ and known T_g	Radiation balance equation	Fourier equation, Force-restore method	Bulk formula	Residual term
Application 4				
Unknown θ and known T_g	Radiation balance equation	Fourier equation, Force-restore method	Bulk formula	Bulk formula

Many times θ is unknown and T_g is known. Then H can be calculated on the basis of bulk formula (see Eq. (A.1)), R_n is estimated by RBE, G can be parameterized either by Fourier or force-restore method, and latent heat flux is obtained as a residual term of VSEBE (*Szabó et al.*, 1989; *Dunkel et al.*, 1989; *Kustas et al.*, 1989). In *Table 1*, this is referred to as application 3. In this case, two approaches can be used for estimating sensible heat flux (*Friedl*, 2002): the single-source or one-layer models (*Inoue et al.*, 1990) and the dual-source or two-layer models (*Kustas et al.*, 1996). In the first ones, there is no distinction between the surface temperature of vegetation canopy and soil surface. In two-layer models, radiation and energy balance of vegetation and soil surface is separately treated. These models are more detailed and physically based than the single-layer ones. In both models the bluff body

effect expressed in the form of excess resistance (often noted by kB^{-1} parameter) has to be implemented to parameterize the aerodynamic resistances for heat transfers. In the application 3, surface moisture status can be deduced either from soil water potential (*Soer*, 1980) or from canopy resistance (*Inoue et al.*, 1990). When θ is unknown and T_g is known, *LE* can also be estimated using bulk formulae. This is referred to as the application 4 in *Table 1*. The surface moisture status is mostly inferred from vegetation canopy resistance (*Shuttleworth* and *Gurney*, 1990). As in the former case, both single-source (*Ács*, 2003) and dual-source (*Taconet et al.*, 1986) models can be used.

All of these applications have been made by data obtained from carefully designed field experiments. In situ measurements are usually extended by means of remote sensing techniques. This combination of techniques is common in organizing large scale experiments in scope of World Climate Research Programme (WCRP) and Global Energy and Water Cycle Experiment (GEWEX). On the other hand, there are also measurements of standard climatological or agrometeorological stations. The question arises, whether characteristics of near-surface exchange processes can also be deduced with the aid of VSEBE using climatological or agrometeorological observations. Reasons for applying VSEBE using agrometeorological observations are as follows:

- Atmospheric forcing variables (ground temperature or near-surface air temperature, air temperature, air humidity, and wind speed at reference level) and soil/vegetation parameters are available at 00, 06, 12 and 18 UTC or even more frequently. Soil moisture content measurements in the growing season were also available at agrometeorological stations. These data can be used for both running and validating VSEBE.

- In principle, θ, H and LE can also be estimated by VSEBE which are not 'standard' climatological elements but their knowledge give a new insight into near-surface climate characteristics.

On the basis of all these, the aim of this study is to check whether VSEBE can be successfully applied for estimating surface soil moisture content θ in the growing season using agroclimatological observations. The analysis is performed using data of the Agrometeorological Observatory of the University of Debrecen (Hungary). The application 4 of VSEBE is used to compare estimated θ_{est} and measured θ_{mea} surface soil moisture content. The applicability of the method and the results are analyzed from both meteorological and climatological point of view. In the study, we assumed that there are no advective effects or mesoscale circulation patterns induced by surface discontinuities (*Hupfer* and *Rabe*, 1994). Then the atmosphere can be assumed to be horizontally homogeneous with constant meteorological boundary conditions above a certain height (*Shuttleworth*, 1988).

2. Measurement site and data

The dataset used was measured at the Agrometeorological Observatory of the University of Debrecen. The measurement site is located at the eastern part of Hungary at Hajdúhát (47°37'N; 21°36'E, 112 m asl). The climate is temperate rain climate with continental features. The annual mean temperature is 10.0 °C, while mean annual precipitation sum is 585 mm. The water table is at a depth of 10 m. The soil type is lime covered black loam (chernozem). Basic soil physical properties are presented in *Table 2*. The vegetation is short-cut natural grass.

Table 2. Soil physical properties of the 0–25 cm layer
at the Agrometeorological Observatory of the University of Debrecen

Properties	Values
Sand fraction	37%
Silt fraction	39%
Clay fraction	24%
Bulk density	1400 kg m^{-3}
Specific heat capacity	840 J kg^{-1} K^{-1}
Organic matter	2.8%
Thermal diffusivity	2.09×10^{-7} m^2 s^{-1}
Soil moisture content at saturation (θ_s)	0.47 m^3 m^{-3}
Field capacity soil moisture content (θ_f)	0.36 m^3 m^{-3}
Wilting point soil moisture content (θ_w)	0.15 m^3 m^{-3}

The dataset used refers to the time period 1974–1986. Atmospheric forcing variables (air temperature, humidity, wind speed, wind direction, cloud fraction) and soil temperature were measured at 00, 06, 12, and 18 UTC. The reference level for air temperature and humidity is 2 m, while for wind speed it is 10 m. Soil temperature is measured at depths of 0.02 m, 0.05 m, 0.1 m, 0.2 m, 0.5 m, and 1.0 m. Both air and soil temperatures are observed by platinum resistance thermometers by accuracy of 0.2 °C. Air humidity is measured by psychrometer using platinum resistance thermometers. Precipitation is measured twice a day, at 06 and 18 UTC. Soil moisture content is measured roughly once a week using gravimetric method. The soil samples are taken from three locations being a few meters far from each other. Samples refer to layers of 10 cm thickness, except the first layer, up to a depth of 1 m. From the surface layer, the samples are taken from 0–5 cm and 5–10 cm layers.

3. Model

The VSEBE model represents a mix of vegetated and bare soil surfaces (*Fig. 1*). It is assumed that vegetation surface is always dry, that is, there is no intercepted water on the vegetation surface. Relative cover of vegetation is *cov*, while of bare soil is 1-*cov*. In VSEBE, there is no difference between vegetation and bare soil surface temperature. Because of the simplicity, the bulk temperature of soil surface layer/vegetation system is modeled. This temperature is called *ground temperature* (T_g).
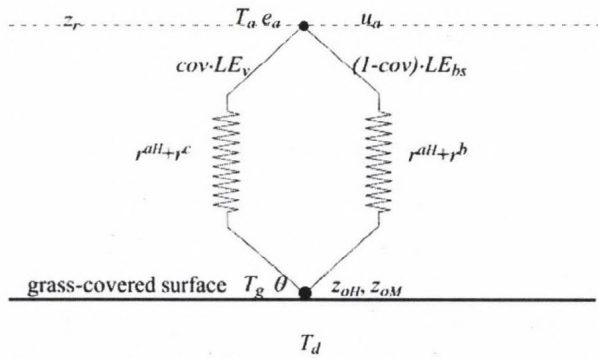
Fig. 1. Surface resistances in the VSEBE model. Symbols: z_r=reference height, T_a=air temperature at z_r, e_a=vapor pressure at z_r, u_a=wind speed at z_r, *cov*=fractional vegetation cover, LE_v=latent heat flux from vegetation, LE_b=latent heat flux from bare soil, r^{aH}=aerodynamic resistance for heat, r^c=vegetation canopy resistance, r^b=soil surface resistance, T_g=ground surface temperature, θ=surface soil moisture content, T_d=deep soil temperature, z_{OH}=roughness length for heat, and z_{OM}=roughness length for momentum.

We also assumed that the soil temperature at 10 cm depth and the soil surface moisture content of vegetated and bare soil surface fractions do not differ. Roughness length is treated as a single effective (*Taylor,* 1995) surface parameter valid for the soil-vegetation system, because the characteristic length scale of bare soil fractions is relatively small to vegetation height (*Blümel,* 1999). Surface temperature is also treated as a single effective quantity, since for sparse canopy both the vegetated and bare soil fractions are active at the surface/atmosphere interface. Based on these assumptions, the aerodynamic resistance is calculated for the soil-vegetation system. The surface resistances of vegetation and soil are calculated separately.

The core of the model is the surface energy balance equation:

$$R_n[T_g(\theta)] - G[T_g(\theta)] - L \cdot E[T_g(\theta)] - H[T_g(\theta)] = F[T_g(\theta)] = 0. \qquad (1)$$

Note that all terms depend via T_g upon θ. This θ-dependence is important feature of VSEBE. It can be used for determining θ when T_g is mostly governed by evapotranspiration, for instance in strong unstable conditions. The model uses atmospheric boundary conditions, soil temperatures, and soil parameters (e.g., roughness length, soil texture or soil hydraulic parameters) as input. The outputs are the estimated turbulent fluxes and surface soil moisture content θ_{est}. Net shortwave radiation is estimated parameterizing global radiation and prescribing albedo of vegetated and bare soil surfaces. Global radiation is parameterized on the base of Kasten's formula after *Holtslag* and *van Ulden* (1983) as well as *Mészáros* (2002). Atmospheric emissivity is parameterized after *Brunt* (1932), while emissivity of the surface is taken to be 1 because of the simplicity. The turbulent heat fluxes are parameterized by bulk formulae. The surface and aerodynamic transfers are simulated by using resistance representation. The vegetation surface resistance is parameterized by *Jarvis* (1976) formula. The moisture availability function F_{ma} is expressed via soil moisture content θ using Theta-parameterization (*Ács*, 2003). The bare soil surface resistance is estimated after *Dolman's* (1993) empirical formula. The aerodynamic transport is simulated by Monin-Obukhov's similarity theory taking into account the atmospheric stability (*Ács* and *Kovács*, 2001). The thermal conductivity is simulated by using $\lambda(\theta) = k\, C(\theta)$ formula (k is the thermal diffusivity, C is the volumetric heat capacity). The thermal diffusivity is estimated on the base of measurement results of *Szász* (1964). Soil physical and hydraulic properties are presented in *Table 2*. The most important parameterizations are given in the Appendix.

As already mentioned, the model is applied only in unstable conditions. The calculation algorithm is schematically presented in *Fig. 2*. T_g is governed to a great extent by $LE(\theta)$ via $r^c(\theta)$, and/or $r^b(\theta)$, and $r^a(T_g - T_a)$. T_g is calculated for each $0 < \theta < \theta_s$ in steps of $\Delta\theta = 0.01$ m³ m⁻³. For a given θ value, the computation always starts from neutral stratification with $T_g = T_a$. The new estimate of T_g is obtained calculating r^{aH} and solving the energy balance equation. This estimate of T_g is used again to improve the estimate of r^{aH}, and so on. In general no more than 5–10 iterations are needed to achive the convergence in successive values of T_g. The surface soil moisture content θ_{est} is obtained simply by

$$\theta = \theta_{est} \quad \text{for} \quad T(\theta) = T_{mea}, \tag{2}$$

where T_{mea} represents a '*measured ground temperature*' obtained by extrapolating measured soil temperatures at 2 and 5 cm depths. θ_{est} refers to the depth of root-zone of grass-covered surface, that is to about 0–20 cm soil surface layer.
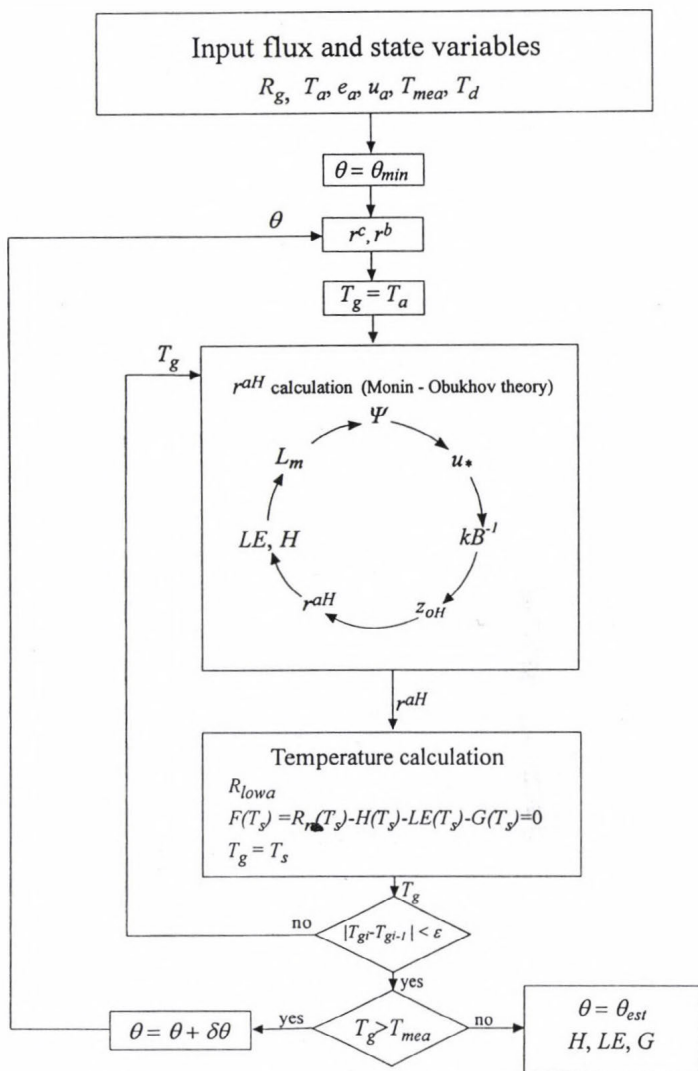
Fig. 2. Flow chart of calculation in the VSEBE model in one time step. Symbols: R_g=global radiation, T_a=air temperature, e_a=water vapor pressure, u_a=wind speed, T_{mea}=ground surface temperature extrapolated by measured soil temperatures at 2 and 5 cm depths, T_d=measured soil temperature at 10 cm depth, r^c=vegetation canopy resistance, r^b=bare soil surface resistance, r^{aH}=aerodynamic resistance for heat transport, ψ=stability function, u_*=friction velocity, $kB^{-1}=\ln(z_{0M}/z_{0H})$, z_{0M}=roughness length for momentum, z_{0H}=roughness length for heat, LE=latent heat flux, H= sensible heat flux, L_m=Monin-Obukhov length, R_{lowa}=long wave radiation from the atmosphere, T_s=surface temperature, ε=arbitrarily chosen small number, $\Delta\theta$=increment of θ, θ_{est} = estimated θ, and G = soil heat flux at the surface.

4. Results

Results are discussed analyzing the applicability of the method, and the goodness of results comparing the estimates (θ_{est}) and measurements (θ_{mea}). The discussion of instantaneous and monthly mean values is separately performed.

4.1 Applicability of the method

Successful application of the method is limited by the meteorological conditions. As briefly discussed in a former study of *Drucza* and *Ács* (2004), the method is mainly applicable for clear-sky (0/8 or 1/8 cloud fraction) and strongly unstable conditions, when soil moisture content θ is less than field capacity θ_f and greater than wilting point θ_w. Consequently, in this study θ-estimates refer only to 12 UTC. The θ-estimates are analyzed with more attention inspecting the relationship between $\delta\theta=(\theta_{est}-\theta_{mea})/\theta_{mea}$, global radiation R_g, and the θ_{mea}. The scatter of these points is presented in *Fig.* 3.
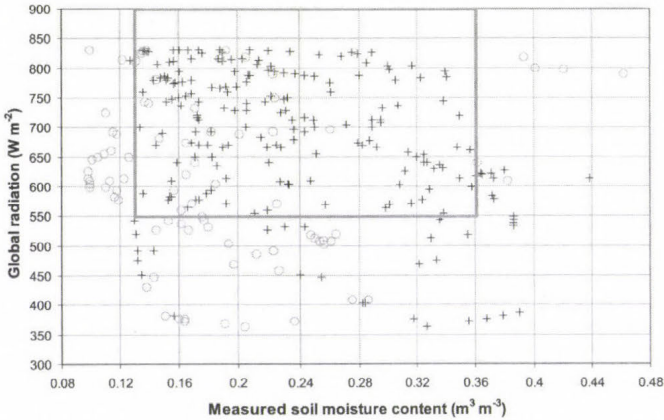
Fig. 3. Applicability of VSEBE for estimating θ as function of measured θ and global radiation. For applicable cases signed by +, $|\theta_{est} - \theta_{mea}| < 30\%$. O indicates not applicable cases. The limits of applicability ($R_g > 550$ W m^{-2} and 0.13 m^3 m^{-3} < $\theta_{mea} < 0.36$ m^3 m^{-3}) are indicated by a grey rectangle.

A brief statistics referring to the scattering of these points is given in *Table 3*. Black + signs represent applicable, while grey o signs refer to not-applicable cases. In the analysis, those cases are treated as applicable when $\delta\theta < 30\%$. This criterion is subjectively chosen. Inspecting *Fig.* 3, it is obvious that applicable and not-applicable cases cannot be clearly separated. Nevertheless, most of the applicable cases lie in θ-region between θ_f (0.36 m^3 m^{-3}) and θ_w (0.13 m^3 m^{-3}) when R_g is strong (above 550 W m^{-2}). This region is indicated by a grey rectangle in *Fig.* 3. The method is not-applicable for extreme dry

and wet conditions, since then the sensitivity of transpiration to soil moisture content is too small. Note that parameterization of R_g refers to clear-sky conditions. R_g is greater than 550 W m^{-2} at 12 UTC from March 11 to September 24.

Conditions/cases	Applicable cases $\delta\theta < 30\%$	Not-applicable cases $\delta\theta > 30\%$	Total
0.13 m^3 m^{-3}< θ_{mea} < 0.36 m^3 m^{-3} and R_g > 550 W m^{-2}	167	25	192
0.13 m^3 m^{-3}> θ_{mea} or θ_{mea}>0.36 m^3 m^{-3} or R_g<550 W m^{-2}	40	57	97
Total	**207**	**82**	**289**

4.2 Instantaneous values

The relationship between the estimated θ_{est} and measured θ_{mea} surface soil moisture content is presented in *Fig. 4*. The scattering of points is obvious, but the correlation coefficient is still acceptable. There are many causes for scattering. They are caused by inadequacies in measurements and theory. Concerning the measurements, following facts have to be mentioned: (a) forcing variables are represented by instantaneous values, (b) θ_{est} refers to 12 UTC, while θ_{mea} is usually determined during the morning, (c) among θ_{mea} values there are also interpolated ones, because θ_{mea} is usually measured in 7–10 days intervals, and (d) the spatial variability of θ_{mea} can be significant. The methodological shortcoming can be deduced comparing *Figs. 5, 6,* and *7. Figs. 5* and *6* represent the sensible and latent heat fluxes, respectively, referring to θ_{est} and θ_{mea}. Note, that the agreement between H_{est} and H_{mea} is somewhat better (R^2=0.71) than that between LE_{est} and LE_{mea} (R^2=0.56). *Fig. 7* represents surface temperatures referring to θ_{est} and θ_{mea}. It is to be noted, that the agreement between T_{est} and T_{mea} is very good (R^2=0.90). Inspecting either the *LE* and *T* (*Figs. 6* and *7*) or *H* and *T* (*Figs. 5* and *7*) plots, it is obvious that scattering of *T* is much smaller than scattering of *LE* or *H*; that is for an acceptable *T*-agreement there is a weaker *LE*- or *H*-agreement. The scatter of *LE* and *H* is determined by scatter of θ. Scattering of θ is determined by slope $S = \delta T(\theta)/\delta\theta$ in the transition region between θ_f and θ_w. *S* is the measure of nonlinear relationship between T and θ. The smaller the slope of $T(\theta)$ curve is, the greater the scattering of θ will be. This physically determined feature of $T(\theta)$ curve basically limits the accuracy of simulations.
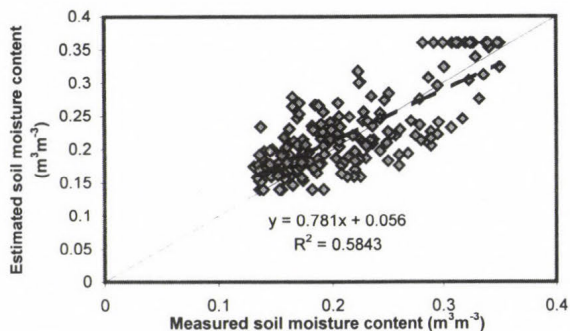
Fig. 4. Estimated versus measured soil moisture content in the surface 0-20 cm layer for the applicable cases (the estimates are obtained at 12 UTC for 0/8 and 1/8 cloud fraction, $R_g > 550$ W m^{-2}, and 0.13 m^3 m^{-3} $< \theta_{mea} < 0.36$ m^3 m^{-3}), in the 1974–1986 period. The regression line fitted is also indicated.
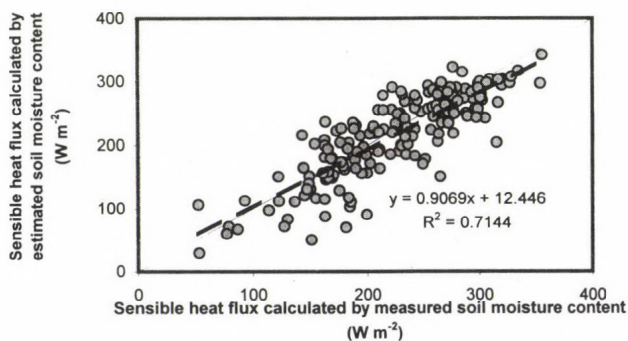
Fig. 5. Sensible heat flux calculated by θ_{est} versus sensible heat flux calculated by θ_{mea} in the 1974–1986 period.
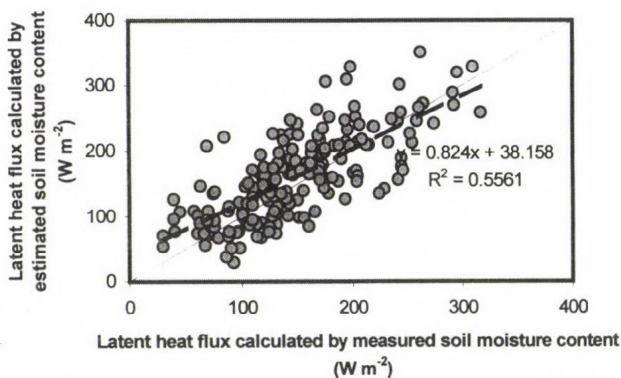
Fig. 6. Latent heat flux calculated by θ_{est} versus latent heat flux calculated by θ_{mea} in the 1974–1986 period.
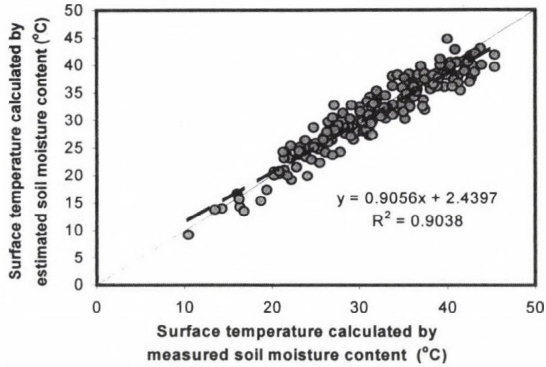
Fig. 7. Surface temperature calculated by θ_{est} versus surface temperature calculated by θ_{mea} in the 1974–1986 period.

Yearly course of θ_{est} and θ_{mea} values in 1976 is presented in *Fig. 8*. The main tendencies of θ_{mea} changes are captured, but there are also obvious discrepancies between θ_{est} and θ_{mea}. The tendency of θ_{mea} changes from March to May is unequivocally reproduced. The local maximum of θ_{mea} in June is also reproduced as well as its continuous decreasing up to August. The greatest discrepancies amount to in average 0.05 m³ m⁻³ and usually appear in extreme moist (in vicinity of θ_f) and dry (in vicinity of θ_w) conditions, when the applicability and thus the accuracy of the method is limited.
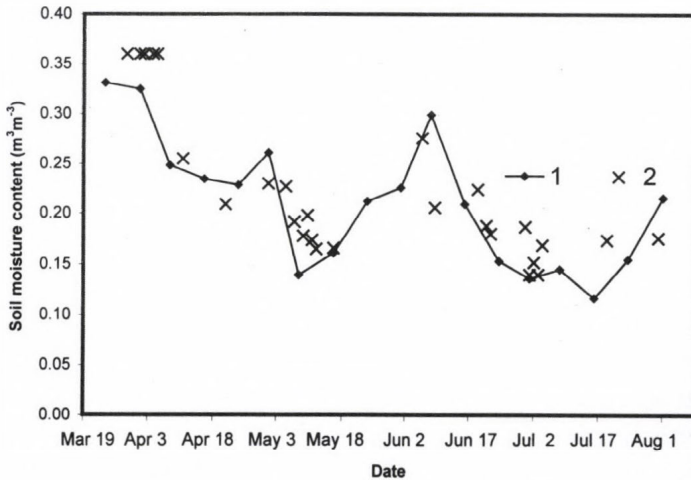
Fig. 8. Annual change of θ_{est} and θ_{mea} in the growing season of 1976. Symbols: (1) measured θ in 0–20 cm layer, (2) estimated θ.

81

4.3 Monthly mean values

From instantaneous θ_{est} and θ_{mea} values, their 12 years monthly mean values are calculated from March to September. 12 years monthly mean values of θ_{mea} are calculated in two ways: For the chosen month, θ_{mea}^{sel} monthly mean value is obtained from those θ_{mea} values, when the method was applicable. In spite of this, θ_{mea}^{all} monthly mean value is obtained using all θ_{mea} values, irrespective of that the method was applicable or not. The relationship between 12 years monthly means of $\cdot\theta_{est}$ and θ_{mea}^{sel} is presented in *Fig. 9a*. The agreement is excellent, namely the slope of the straight line obtained ($\theta_{est}=0.95\ \theta_{mea}^{sel}+0.017$) is 0.95. In March, θ is about 0.30 m³ m⁻³. In April, θ is somewhat smaller than in March, it amounts to about 0.25 m³ m⁻³. In May, θ is about 0.20 m³ m⁻³. Note, that θ values in June, July, August, and September are located close to each other and they are not significantly different from θ values obtained in May.
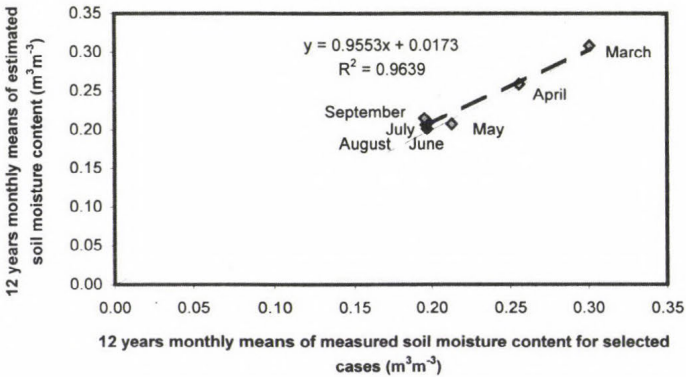
Fig. 9a. 12 years monthly means of θ_{est} versus 12 years monthly means of θ_{mea}^{sel}.
For the chosen month, θ_{mea}^{sel} represents the average of those θ_{mea},
when the method was applicable.

The relationship between 12 years monthly means of θ_{est} and θ_{mea}^{all} is presented in *Fig. 9b*. The agreement between θ_{est} and θ_{mea}^{all} is acceptable. The slope of straight line obtained ($\theta_{est}=0.71\ \theta_{mea}^{all}+0.048$) is 0.71, that is θ_{est} values are somewhat underestimated with respect to θ_{mea}^{all} values. The points show greater scattering than in the former case, but the strength of the relationship is still acceptable ($R^2=0.73$). θ is the greatest (about 0.30–0.33 m³ m⁻³) in March decreasing in spring (April: about 0.25–0.30 m³ m⁻³, May: about 0.20–0.27 m³ m⁻³, and June: about 0.19–0.25 m3 m-3). In July, θ is about 0.20–0.23 m³ m⁻³. The smallest values appear in August and September, they amount to about 0.20 m³ m⁻³ in accordance with expectations.
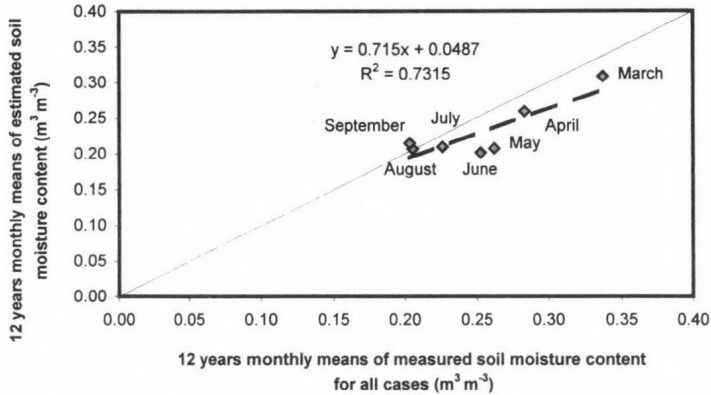
Fig. 9b. 12 years monthly means of θ_{est} versus 12 years monthly means of θ_{mea}^{all}. For the chosen month, θ_{mea}^{all} represents the average of all θ_{mea}, irrespective of that the method was applicable or not.

5. Conclusions

A diagnostic application of VSEBE for estimating surface soil moisture content θ is presented. We tested whether VSEBE can be successfully applied using agroclimatological observations. The analysis is performed using data of the Agrometeorological Observatory of the University of Debrecen collected in the period 1974–1986. The main findings are as follows:

- The applicability of VSEBE is determined by both the atmospheric stability and surface wetness state. The method is mainly applicable for clear-sky (0/8 or 1/8 cloud fraction) and strongly unstable conditions, when θ_{mea} is between θ_f and θ_w.

- The agreement between instantaneous values of θ_{est} and θ_{mea} is acceptable even if the scattering of points is relatively large. In spite of the scattering of instantaneous values, the 12 years monthly mean values of θ_{est} and θ_{mea} agree well. Note, that the agreement between θ_{est} and θ_{mea}^{sel} is excellent, while the agreement between θ_{est} and θ_{mea}^{all} is weaker. In this latter case, θ_{est} is somewhat underestimated with respect to θ_{mea}^{all}.

The results suggest that VSEBE cannot be successfully applied for estimating instantaneous θ values using agroclimatological observations. The successful applications are strongly limited and the scattering of the estimates is relatively large. Nevertheless, it is possible to estimate monthly mean values of θ with acceptable accuracy applying VSEBE in a long time period and grouping θ values according to months, as it is done in this study. That is, VSEBE can be

applied for climatological estimates using agroclimatological observations. The procedure is quite extensive, but in this way the non-linear effects are taken into account. In this case, it is strongly recommended to compare measurements and estimates, that is, to validate the model. Accordingly, VSEBE cannot be used for inferring monthly mean θ fields in Hungary, since there are only a few stations (for instance Keszthely, Kecskemét-Katonatelep, Karcag, and Debrecen-Pallag) possessing long time θ series (*Erdős és Morvay*, 1961). If we want to avoid the enormous data processing, that is the scaling up of outputs in time and space, the production of monthly mean θ fields has to be done on daily or monthly time scale using relevant variables. In most cases these are monthly values of precipitation and temperature, as it is done for instance by *Thornthwaite* (1948).

APPENDIX

Parameterizations used in VSEBE

Turbulent heat fluxes:

$$H = \rho \cdot c_p \cdot \frac{T_g - T_a}{r^{aH}}, \tag{A.1}$$

$$LE = \frac{\rho \cdot c_p}{\gamma} \cdot \frac{e_s(T_g) - e_a}{r^{aH} + r^s}, \tag{A.2}$$

ρ [kg m^{-3}] is the air density, c_p [J kg^{-1} K^{-1}] is the specific heat capacity of air at constant pressure, T_g [°C] is the ground surface temperature, T_a [°C] is the air temperature at 2 m height, r^{aH} [s m^{-1}] is the aerodynamic resistance for heat, γ [hPa K^{-1}] is the psychrometric constant, $e_s(T_g)$ [hPa] is the saturation vapor pressure at T_g, e_a [hPa] is the vapor pressure at 2 m height, r^s [s m^{-1}] indicates the surface resistance of bare soil (r^b) or vegetation canopy (r^c). The fluxes are positive upwards and negative downwards.

Ground heat flux:

Ground heat flux is approached by Fourier equation:

$$G = \lambda \frac{T_{s5} - T_{s10}}{z_5 - z_{10}}, \tag{A.3}$$

where λ [W m^{-1} K^{-1}] is the thermal conductivity, $z_5 = 5$ cm, $z_{10} = 10$ cm, T_{s5} [°C] is the soil temperature at z_5, and T_{s10} [°C] is the soil temperature at z_{10}. The soil heat flux is positive downwards and negative upwards.

Roughness length for momentum and zero plane displacement height:

The roughness length for momentum transfer (z_{0M} [m]) and zero plane displacement height (d[m]) is expressed as the function of vegetation height (*vegH* [m]) after *Brutsaert* (1982):

$$z_{0M} = 0.136 \cdot vegH \,, \tag{A.4}$$

$$d = 0.667 \cdot vegH \,. \tag{A.5}$$

Roughness length for heat and/or vapor transfer:

Roughness length for heat and/or vapor transfer (z_{0H} [m]) is parameterized after *Kustas et al.* (1989):

$$kB^{-1} = \ln \frac{z_{0M}}{z_{0H}} \,, \tag{A.6}$$

$$kB^{-1} = 0.17 u_a (T_g - T_a) \,, \tag{A.7}$$

where u_a [m s^{-1}] is the wind speed and T_a [°C] is the air temperature at reference height, T_g [°C] is the ground surface temperature.

Surface resistances:

Vegetation canopy resistance is parameterized after *Jarvis'* (1976):

$$r^c = \frac{r_{st\,min} \cdot F_{ad}}{LAI \cdot GLF \cdot F_{ma}} \,, \tag{A.8}$$

where r_{stmin} [s m^{-1}] is the minimum stomatal resistance, *LAI* is the leaf area index, *GLF* is the green leaf fraction; it expresses the fraction of live leaves ranging between 0 and 1, F_{ad} and F_{ma} represent the atmospheric demand and soil moisture availability effect on stomatal functioning, respectively, ranging between 0 and 1.

F_{ma} is parameterized via volumetric soil moisture content (θ, [m^{3}m^{-3}]), field capacity (θ_f [m^3 m^{-3}]), and wilting point θ_w [m^3 m^{-3}]:

$$F_{ma} = \min\left(\frac{\theta - \theta_w}{\theta_f - \theta_w}, 1\right).$$

(A.9)

The soil surface resistance [s m^{-1}] is parameterized after *Dolman* (1993):

$$r^b = 3.5 \cdot \theta^{-2.3}.$$

(A.10)

List of Symbols

C	volumetric heat capacity of soil
cov	vegetated fraction of surface
c_p	specific heat capacity of air at constant pressure
d	zero plane displacement height
e_a	vapor pressure at reference height
$e_s(T_g)$	saturation vapor pressure at T_g,
F_{ad}	atmospheric demand function
F_{ma}	moisture availability function
G	soil heat flux at the surface
GLF	green leaf fraction
H	sensible heat flux
H_{est}	estimated sensible heat flux
H_{mea}	measured sensible heat flux
k	soil thermal diffusivity
kB^{-1}	excess resistance term for heat transfer
LAI	leaf area index
LE	latent heat flux
LE_{est}	estimated latent heat flux
LE_{mea}	measured latent heat flux
r^a	aerodynamic resistance
r^{aH}	aerodynamic resistance for heat
r^b	surface resistance of bare soil
RBE	radiation balance equation
r^c	surface resistance of vegetation canopy
R_n	net radiation
r^s	surface resistance of bare soil (r^b) or vegetation canopy (r^c).
r_{stmin}	minimum stomatal resistance
S	slope of the $T(\theta)$ curve
T_a	air temperature at reference level
T_g	ground surface temperature
T_{mea}	measured ground temperature obtained by extrapolating measured soil temperatures at 2 and 5 cm depths
u_a	wind speed at reference height
$vegH$	vegetation height ($vegH$ [m])
$VSEBE$	energy balance equation for vegetated surface
z_{0M}	roughness length for momentum transfer
γ	psychrometric constant
δ	difference between measured and estimated surface soil moisture content

θ_{est} estimated soil moisture content
θ_f soil moisture content at field capacity
θ_{mea} measured soil moisture content at 0–20 cm layer
θ_{mea}^{all} monthly mean value of all θ_{mea}
θ_{mea}^{sel} monthly mean value of selected θ_{mea} (averaging θ_{mea} when θ_{est} is available)
θ_w soil moisture content at wilting point
λ soil thermal conductivity
ρ air density

References

Ács, F., *Mihailovic, D.T.*, and *Rajkovic, B.*1991: A Coupled Soil Moisture and Surface Temperature Prediction Model. *J. Appl. Meteorol. 30*, 812-822.

Ács, F., *Hantel, M.*, and *Unegg, J.W.*, 2000: Climate Diagnostics with the Budapest-Vienna Land-Surface Model SURFMOD. *Austrian Contribution to the IGBP. Vol. 3, National Committee for the IGBP, Austrian Academy of Sciences*, 116 pp.

Ács, F. and *Kovács, M.*, 2001: The surface aerodynamic transfer parameterization method SAPA: description and performance analyses. *Időjárás 105*, 165-182.

Ács, F., 2003: A comparative analysis of transpiration and bare soil evaporation. *Bound. - Lay. Meteorol. 109*, 139-162.

Bhumralkar, C.M. 1975. Numerical experiments on the computation of ground surface temperature in an atmospheric general circulation model. *J. Appl. Meteorol.* 14, 1246-1258.

Blümel K., 1999: A simple formula for estimation of the roughness length for heat transfer over partly vegetated surfaces. *J. Appl. Meteorol. 38*, 814-829.

Brunt, D., 1932: Notes on radiation in the atmosphere. *Q. J. Roy. Meteor. Soc. 58*, 389-420.

Brutsaert, W., 1982. *Evaporation into the Atmosphere*. D. Reidel, 299 pp.

Dolman, A.J., 1993: A multiple-source land surface energy balance model for use in general circulation models. *Agr. Forest Meteorol.* 65, 21-45.

Drucza, M. and *Ács, F.*, 2004: On the use of energy-balance model for estimating soil moisture content (in Hungarian). In *Forests and Climate, IV tome* (ed.: *Cs. Mátyás*), Nyugat-Magyarországi Egyetem, Sopron, 123-132.

Dunkel, Z., *Bozó, P.*, *Szabó, T.*, and *Vadász, V.*, 1989: Application of thermal infrared remote sensing to the estimation of regional evapotranspiration. *Adv. Space Res. 9*, (7)255-(7)258.

Erdős, L. and *Morvay, A.*, 1961: Soil moisture course of some soil types (in Hungarian). *Időjárás 65*, 47-55.

Friedl, M.A., 2002: Forward and inverse modelling of land surface energy balance using surface temperature measurements. *Remote Sens. Environ. 79*, 344-354.

Holtslag, A.A.M. and *Ulden, A.P.V.*, 1983: A simple scheme for daytime estimates of the surface fluxes from routine weather data. *J. Clim. Appl. Meteorol. 27*, 689-704.

Hupfer, P. and *Raabe, A.*, 1994: Meteorological transition between land and see in the microscale. *Meteorol. Z. 3*, 100-103.

Inoue Y., *Kimball, B.A.*, *Jackson, R.D.*, *Pinter, P.J.*, and *Reginato, R.J.*, 1990: Remote estimation of leaf transpiration rate and stomatal resistance based on infrared thermometry. *Agr. Forest Meteorol. 51*, 21-33.

Jarvis, P.G., 1976: The interpretation of the variations in the leaf water potential and stomatal conductance found in canopies in the field. *Philos. Trans. Roy. Soc., Ser. B. 273*, 593-610.

Kustas, W.P., *Choudhury, B.J.*, *Moran, M.S.*, *Reginat, R.J.*, *Jackson, R.D.*, *Gay, L.W.*, and *Weawer, H.L.*, 1989: Determination of sensible heat flux over sparse canopy using thermal infrared data. *Agr. Forest Meteorol. 44*, 197-216.

Kustas, W. P., Humes, K. S., Norman, J. M., and *Moran, M. S.*, 1996: Single- and Dual-Source Modelling of Surface Energy Fluxes with Radiometric Surface Temperature. *J. Appl. Meteorol. 35*, 110-121.

Mészáros, R., 2002: Dry deposition of ozone over different surface types (in Hungarian). *PhD. Thesis*, pp.111.

Shuttleworth, J.W., 1988: Macrohydrology-the new challenge for process hydrology. *J. Hydrol. 100*, 31-56.

Shuttleworth, J.W. and *Gurney, R.*, 1990: The theoretical relationship between foliage temperature and canopy resistance in sparse crops. *Q. J. Roy. Meteor. Soc. 116*, 497-519.

Soer, G.J.R., 1980: Estimation of regional evapotranspiration and soil moisture conditions using remotely sensed crop surface temperatures. *Remote Sens. Environ. 9*, 27-45.

Szabó, T., Tóth, R., Csapó, P., Tiringer, Cs., and *Lambert, K.*, 1989: Estimation of evapotranspiration of wheat canopy under dry soil conditions using surface temperature data. *Időjárás 93*, 253-260.

Szász, G., 1964: Measurement of diurnal change of the thermal conductivity (in Hungarian). *Agrokémia és Talajtan 13*, 137-148.

Taconet, O., Bernard, R., and *Vidal-Madjar, D.*, 1986: Evapotranspiration over an agricultural region using a surface flux/temperature model based on NOAA AVHRR data. *J. Clim. Appl. Meteorol. 25*, 284-307.

Taylor C.H., 1995: Aggregation of wet and dry surfaces in interception schemes for General Circulation Models. *J. Climate 8*, 441-448.

Thornthwaite, C.W., 1948: An approach toward a rational classification of climate. *Geogr. Rev. 38*, 55-89.

van de Griend, A.A., Camillo, P.J., and *Gurney, R..J.*, 1985: Discrimination of soil physical parameters, thermal inertia, and soil moisture from diurnal surface temperature fluctuations. *Water Resour. Res. 21*, 997-1009.

Downscaling EPS probabilities using SYNOP precipitation data

Ervin Zsótér

Hungarian Meteorological Service[*],
P.O. Box 38, H-1525 Budapest, Hungary; E-mail: ervin.zsoter@ecmwf.int

Abstract—The probability forecasts of precipitation (PoP) are of great interest in numerical weather forecasting. Besides the model errors and the ensemble spread insufficiencies, the quality of these PoP forecasts is strongly affected by the problem of representativity: while the original forecasts are valid on the scale of a gridbox, we want to verify them with observations of local stations. These inconsistencies can be treated by the so-called upscaling and downscaling methods. This paper presents a new approach for downscaling PoP forecasts with the combination of the esemble prediction system (EPS) and the representativity conditions explored by conditional error statistics of the observations with respect to forecasts.

Regarding the probability density functions (PDF) of the observations respect to the different forecast values, we found that there is only a very small difference between two or three years seasonal PDF-s as long as the model environment was consistent, and the geographical variability of the PDF-s is also not significant between areas – like Central Europe and Northern Hemisphere.

The new downscaling method in general delivered better verification statistics than the operational one. The best results could have been obtained for winter, while the least improvement was attained for summer. While the old probabilities were underconfident for most of the cases, the new probabilities showed some overconfidency. In general, there is no significant improvement in the resolution, but as an important result there is no deterioration at all. The greatest improvement was gained for the Brier skill score, especially for the thresholds of 1 mm and 5 mm. Regarding ROC curves, higher hit rates were also present, mainly for bigger thresholds. In addition strong similarities were found between the results for JJA and MAM, and also in the case of DJF and SON, which can probably be explained by local scale convection.

Key-words: ensemble forecast, probability distribution function, representativity error, Brier score, relative operating characteristics

---

[*] Present address: European Centre for Medium-Range Weather Forecasts (ECMWF), Shinfield Park, Reading, RG2 9AX, England

1. Introduction

Since the beginning of the 1990's, the probabilistic way of forecasting weather events has become more and more widespread (*Ehrendorfer,* 1997). Nevertheless, one of the most important tasks is the numerical forecasting of precipitation. To obtain comprehensive knowledge of the forthcoming weather scenarios regarding extreme events of rain and snow, probability forecasts are essential. The numerical forecast systems provide predictions – deterministic and probabilistic – directly for the scale of a grid-box. However, it is of great importance to know the accurate probability of the occurrence of weather events not only for a whole grid-box, but for any local point inside that grid-box. This paper presents a new approach for creating local probabilities with the combination of the EPS and representativity conditions explored by conditional error statistics of the observations with respect to forecasts.

When dealing with probabilistic forecasts in general, three types of errors have to be considered. At first, the atmospheric model is not perfect, so errors are likely to rise because of the physical or dynamic inconsistencies with the true atmosphere. Additionally, on many occasions the ensemble spread is not large enough, so the verifying observations are below or above all of the ensemble members, therefore, the perturbations of the initial state do not completely represent the real uncertainty of the atmosphere (*Hamill*, 2000). Finally, the problems associated with representativity have to be addressed. This arose from the fact that the forecast represents a grid-box value, while the verifying observations indicate local occurrences. The spatial scale of the grid-box is on the order of 1000 km^2, while the representative scale of raingauges is only a fraction of 1 m^2. Therefore, the quality of the forecast is highly dependent on the accidental choice of the particular local point (one or more) within the grid-box as a verifying station. The idea of this research concerns the representativity error. The reason why the operational PoP predictions strongly overforecast the precipitation at local observations might be the representativity error as well as, for example, model bias or lack of ensemble spread.

To deal with the representativity problem, two different methods can be identified. The first is called upscaling. In this method a representative observation value is created for every grid-box using as many local observations of the grid-box as possible (*Ghelli* and *Lalaurette*, 2000). In contrast, the downscaling method works in the opposite direction, we start from a grid-box forecast value and derive the probability forecast for the scale of local stations. Before describing our improved way for downscaling, we review two important ways of deriving PoP forecasts in general.

The first method is a simple conditional statistical analysis. The distributions of observations gathered over a long period are determined for every individual forecast or forecast interval. This could be interpreted by a set of cumulative probability distribution functions (PDF),

$$P(obs < x \mid f) = PDF_f(x),$$ (1)

where f is the forecast and x is the threshold. Here each PDF represents the probability distribution of observations below a certain threshold, knowing that the forecast was f.

A second method is to use an ensemble prediction system (EPS) (*Palmer et al.*, 1992). In the frame of the EPS we transform a prescribed distribution of initial errors into the future. This means that many possible weather outcomes can result from only a slight variation in the initial state of the atmosphere. At the time of this study, at the European Centre for Medium-Range Weather Forecasts (ECMWF) 50 perturbed forecasts were run operationally at T255 horizontal resolution with 40 vertical levels (L40). To obtain probability values from these 50 perturbed forecasts, a simple operational method was used. Assuming that the 50 members are independent, and each gives an equally probable state of the future weather (the ensemble spread is perfect), the probability of having the observation above a threshold within a certain time frame (usually 24 hours) is equal to the proportion of those ensemble members, which predict more than the threshold value. This method is called the democratic voting method, because every member is equal and they can be only pro or contra to the event. The overall probability can be derived simply by averaging the members' yes or no votes,

$$P(obs > x \mid f_1, f_2, ..., f_{50}) = \frac{1}{50} \cdot \sum_{i=1}^{50} H(f_i - x),$$ (2)

where x is the threshold, f_i is the forecast of the ith member, and $H(v) > 1$, only if $v > 0$.

To emphasize the importance of the representativity problem, an example is presented. Let us have a set of 50 EPS member's quantitative precipitation forecasts, and let the threshold be 5 mm. Assume that every member predicts 10 mm for a grid-box, where we have 20 observations ranging from 1 to 28 mm, four of them being less than 5 mm. In the original procedure, the operational probability would be 100%, knowing that every member is above 5 mm. However, assuming that in the Global Telecommunication System (GTS) there is only one station for that grid-box (and this is the case for most of the grid-boxes), we would have an inbuilt error within our forecast. This would be a

consequence of the fact, that the official verifying observation could be one of the observations within that 20 locally available with less than 5 mm. This suggests that the operational probability of 100% is not correct at the scale of the local stations. The average of the observations within the grid-box could be 10 mm, notwithstanding that the expected local probability of more than 5 mm is less than 100%. In this example we might have forecasted less than 100% if we would have known the fact that statistically there is only approximately 80% of probability having more than 5 mm rain locally, assuming that the forecast for the grid-box was exactly 10 mm.

The underlying new concept is exactly the same what we had presented with the conditional statistical analysis of the observations explained above. Our approach is then to obtain more accurate probabilities using a combination of the ensemble prediction system and the conditional statistical analysis. It would be of great value if we could create a context, in which a problem of representativity could be statistically examined, excluding other errors. If this could be done successfully, we could superimpose the representativity correction onto the ensemble forecasts, producing accurate PoP forecasts on a local scale. The assumption that the EPS members are still independent, makes it possible to write the computation of the new probabilities as follows:

$$P(obs > x \mid f_1, ..., f_{50}) = \frac{1}{50} \cdot \sum_{i=1}^{50} P(obs > x \mid f_i) = \frac{1}{50} \cdot \sum_{i=1}^{50} [1 - P(obs \le x \mid f_i)], \quad (3)$$

where f_i is the ith member's forecast, x is the threshold, and $P(obs \le x \mid f_i) = PDF_{f_i}$ is the cumulative probability distribution function of the observations knowing that the forecast is f_i.

In the following sections the PDF generation procedure and the behavior of these distributions will be described first. Then the property of the new probability fields will be discussed, and finally we present some verification results of the test periods together with a summary.

2. Generation of the probability distribution functions

For the generation of the probability distribution functions (PDFs) described in the introduction, a set of deterministic forecast and SYNOP observation pairs were needed. The ensemble prediction system (EPS) was running at T255L40. To attain the best results possible, the forecast for the statistical analysis had to be chosen consistently with the EPS version. Because of other experiments, the operational deterministic forecast data was available for many years,

interpolated onto the SYNOP station locations. Therefore, it was convenient and time efficient to use the operational forecast. The best fit could have been reached for the year of 2000, when the deterministic forecast was operational at T319L60 with very similar horizontal resolution as the EPS.

To perform the statistical calculations of PDFs, a vast amount of data was needed. It is not possible to apply the method on a relatively small area (e.g., Great Britain), because a very long time period (dozens of years) or data from a lot of stations (thousands) would have been required. The dynamic nature of model algorithm changes means that it is difficult to obtain consistent data over a long period of time. Another problem is the insufficient number of SYNOP stations for small regions.

We wanted to focus on seasonal changes, and an appropriate sample size had a great importance. Therefore the whole season periods (three months) and the extra tropical region of the Northern Hemisphere (between latitudes 30°N and 80°N) were considered. To obtain the deterministic forecast values for the station location, a bilinear interpolation was used. For the experiment only those SYNOP stations were selected, which reported at the frequency of the European stations. Altogether 2000 different stations were selected (*Fig. 1*). Those particular stations, where the 24 hours accumulation could not be obtained for a particular day, were excluded from the survey. For a three-month period we had about $91 \times 2,000 \sim 180,000$ forecast-observation pairs. Because of reporting problems, this number was reduced to about 130,000–40,000 cases for each season.
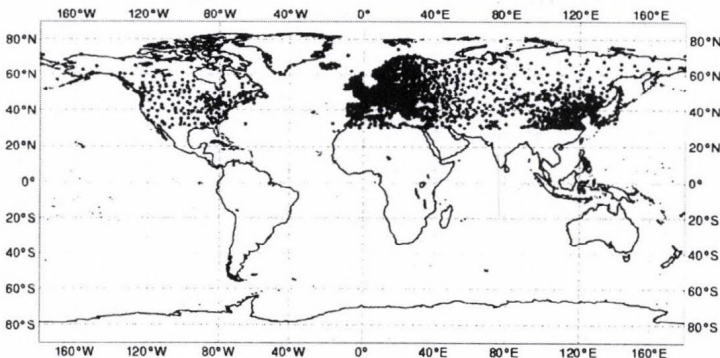
Fig. 1. The selected SYNOP stations over the extra tropical region of the Northern Hemisphere, between 30°N and 80°N.

To give an example data set, a scatter diagram is presented in *Fig. 2*. Ideally PDFs should be generated for every possible precipitation value, but according to the limited sample size, forecast intervals (bins, bounded by

vertical lines in *Fig. 2*) had to be defined instead of the single values. In addition, having too few intervals is also not desirable, because in this case quite large amount of information would be lost when interpolating between two PDF curves in order to get the probability value for an individual forecast.

This interval selection scheme was tested on a number of occasions. To obtain a stable distribution (i.e., to give a representative sample of the reality), ideally we need at least 200–300 observations within one forecast interval. Because high amounts of rain are seldom forecasted, to have stable result, for higher forecast values wider and wider bins had to be defined. For all investigation performed the following stratification intervals were used: 0, 0.1, 0.2, 0.3, 0.4, 0.5–0.8, 0.8–1, 1–2, 2–3, 3–4, 4–5, 5–6, 6–7, 7–8, 8–10, 10–12, 12–15, 15–20, 20–30, 30–50, 50–100, >100 mm. Because of lack of data, at most of the cases we could not

NORTHERN EXTRATROPICS, DJF 1999-2000
(125827 observations and 1541 stations)

18-42h range forecast

Fig. 2. Scatter diagram for winter 1999–2000. The vertical lines are the bounds of some stratifying forecast intervals.

derive any valuable information for the interval of >100 mm, thus an extrapolation was used.

Traditionally, precipitation is accumulated over 24 hours from 06 to 06 UTC, which corresponds to the operational forecast range of 18-42 h. However, because of the need to keep the model error as small as possible in order to catch only the representativity properties, the forecast interval of 06-30 h had to be chosen. At first we undertook the statistical investigation for the whole area (Northern Extra tropics), and for all the seasons in 2000 (with DJF 1999-2000, MAM-2000, JJA-2000, SON-2000). PDF curves presented for the winter of 1999-2000 can be seen in *Fig. 3*. The distribution curve for the 0 mm forecast value is located at the upper left corner, while the rest of the curves follow after each other from the top left to the right, following the order of the stratifying forecast intervals described above (0, 0.1, 0.2, ..., 30-50, 50-100, >100 mm). The PDF curves are rather stepwise, because the observations are not continuous. Most of the cases in SYNOP stations, fractions of mm are not reported. On the diagram the curve of the last forecast interval (50-100 mm) is quite unstable, because we had less than 100 cases to create the distribution (above 100 mm we did not have forecast at all).
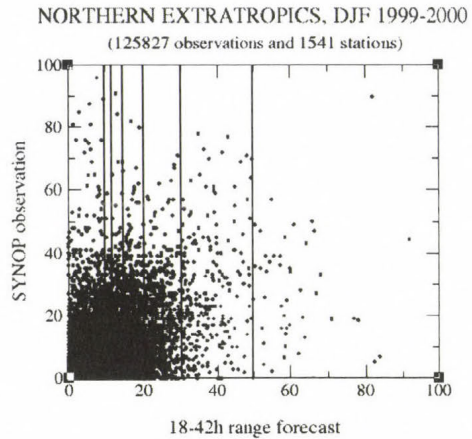
DJF 1999-2000

Fig. 3. Probability distribution functions for different forecast intervals, Northern Hemisphere, winter (DJF) of 1999–2000, forecast step 18–42 h.

In the following paragraphs we present some examinations of the behavior of the PDF curves. At first, the dependence of the PDFs on the chosen forecast ranges was tested. Besides the originally chosen 06–30 h interval, we set up two other periods with forecast ranges of 18–42 h and 90–114 h.

JJA-2000

0 mm (06-30)	0 mm (18-42)	0 mm (90-114)
1-2 mm (06-30)	1-2 mm (18-42)	1-2 mm (90-114)
8-10 mm (06-30)	8-10 mm (18-42)	8-10 mm (90-114)
20-30 mm (06-30)	20-30 mm (18-42)	20-30 mm (90-114)

Fig. 4. Comparison of the PDFs for 06–30 h, 18–42 h and 90–114 h forecast ranges, Northern Hemisphere, JJA-2000, four different forecast intervals.

Fig. 4 shows a typical example for JJA-2000 (hereafter we chose to display 4 representative distribution curves (0 mm, 1–2 mm, 8–10 mm, and 20–30 mm) from all forecast intervals on this kind of diagrams, which follow

after each other always from the top left to the right). The differences among the three sets of curves are significant. In this case the results overlap with our expectations, the shortest range (06–30) gives the sharpest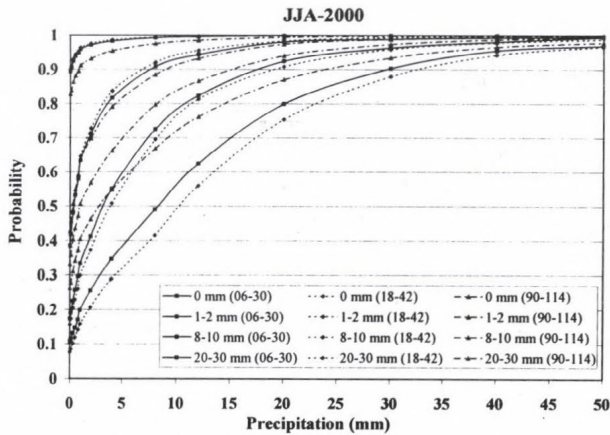 distribution of the observations. For small forecast values a bigger and bigger proportion of the observations are above a threshold as the forecast range increases. For higher forecasts this effect is reversed. After about two weeks, the skill of the forecast system would probably disappear, and the distribution curves would lie on the top of each other for every forecast interval. In the section 4 some comparison among the verification results of these different forecast ranges, 06–30 h, 18–42 h, and 90–114 h will be shown.
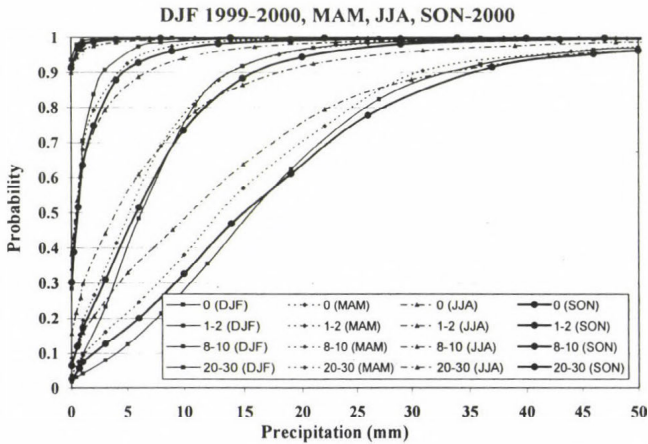
Fig. 5. Comparison of the PDF-s for DJF of 1999–2000, MAM, JJA, and SON of 2000, Northern Hemisphere, 06–30 h, for four different forecast intervals.

The next step in the investigation was to study the interannual and spatial characteristics of the probability distribution curves. In order to accomplish this task, we calculated the PDF curves for each season from MAM 1999 until summer 2001. These seasonal differences can be seen in *Fig. 5*. The curves for the same forecast interval do not match. The possible reasons for these differences are the convection and existence of different weather patterns. As it might be expected, spring and autumn are quite similar, while winter with largescale precipitation, and summer with large proportion of convective rain differ significantly. For small forecast values, the PDF curves for winter indicate just a slight chance of having large amount of precipitation (more than 5 or 10 mm), while regarding big values of forecasts the probability is relatively high. During summer, probably due to the uncertain convection, the opposite can be deducted.

There is another interesting aspect in the behavior of the PDFs, namely the interannual variability. During the seasons from spring of 1999 until the summer of 2001, two basic model changes could have strongly effected the PDFs. First, in October 1999 a change in the cloud and convection scheme took place, and in November 2000, T511 was put into operation. Analyzing the diagrams in *Figs. 6-9* we may conclude, that the change in the precipitation scheme affected the distributions quite strongly. While the latter change in resolution seem to cause just a slight modification. Results from the two winters with different resolution almost exactly overlap. In contrast, the spring and summer show much bigger differences, but the pattern of the deviation is rather similar.
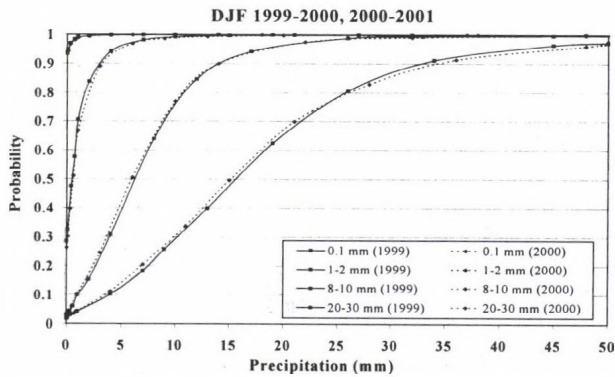
Fig. 6. Comparison of the annual variability of the PDF curves for winter, for four different forecast intervals.
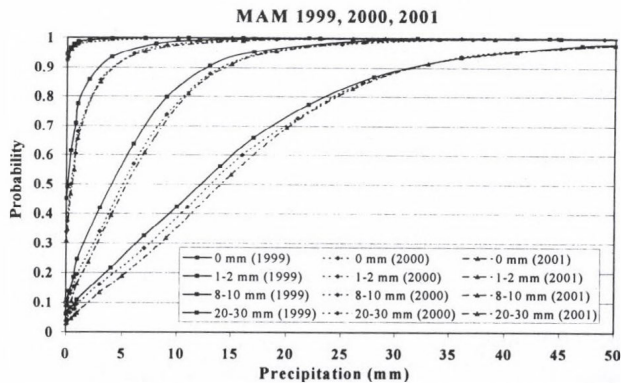
Fig. 7. Comparison of the annual variability of the PDF curves for spring, for four different forecast intervals.
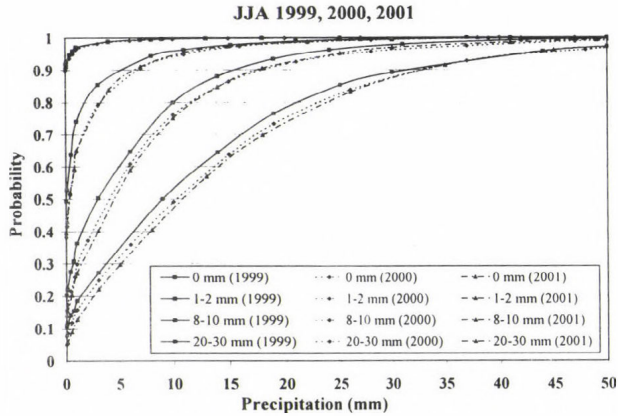
Fig. 8. Comparison of the annual variability of the PDF curves for summer, for four different forecast intervals.
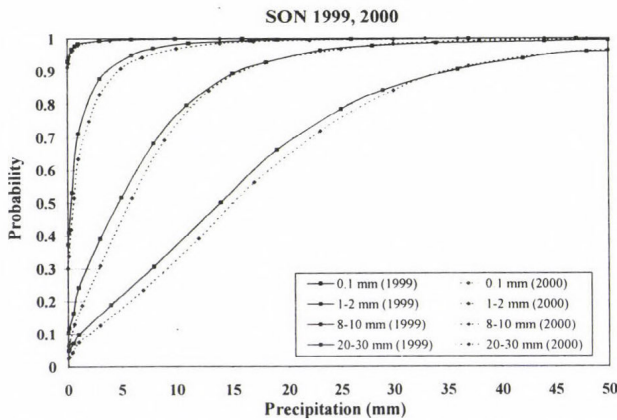
Fig. 9. Comparison of the annual variability of the PDF curves for autumn, for four different forecast intervals.

The curves are quite close in year 2000 and 2001, but during the summer of 1999 – the one with different precipitation scheme – we got significantly different distributions. The frequencies are consequently smaller for every forecast interval.

The spatial variability of the PDF curves is also important. To test the regional differences, we defined three regions besides Northern Hemisphere (NH): the European area (EU), the Northwest part of Europe (NWEU), and Central Europe (CE) (*Fig. 10*).
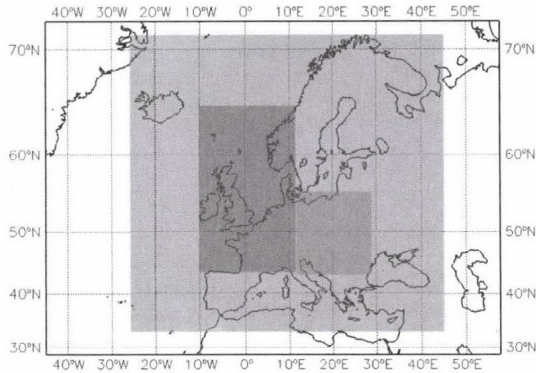
Fig. 10. Location of the geographical regions that are used in the study:
Europe, Northwest Europe, and Central Europe.

We had about 80,000 observations for Europe, 25,000–30,000 for NWEU, and 20,000 for CE (as we stated above it is about 130,000–140,000 for NH). Because of the small sample size, for this comparison two years of data sets were put together. The results for the winter and summer periods can be seen in *Figs. 11* and *12*, respectively.

For winter the forecast distributions are represented by almost the same curves, and the differences are really small. However, regarding the summer PDFs, we could see larger deviations, but the curves still do not lie too far from each other. We could draw almost the same conclusion that we came to on the annual variability of the PDFs. Winter has the best, and summer has the worst overlapping property amongst the seasons.

Fig. 11. Comparison of the spatial variability of the PDF curves for 4 regions – Northern Hemisphere (NH), Europe (EU), Northwest Europe (NWEU), and Central Europe (CE) – for winter season with two years data together, for 4 different forecast intervals.
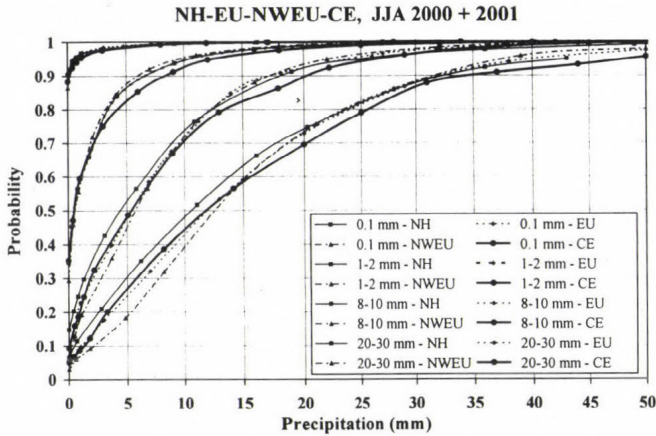
Fig. 12. Comparison of the spatial variability of the PDF curves for 4 regions – Northern Hemisphere (NH), Europe (EU), Northwest Europe (NWEU), and Central Europe (CE) – for summer, with two years data together, for 4 different forecast intervals.
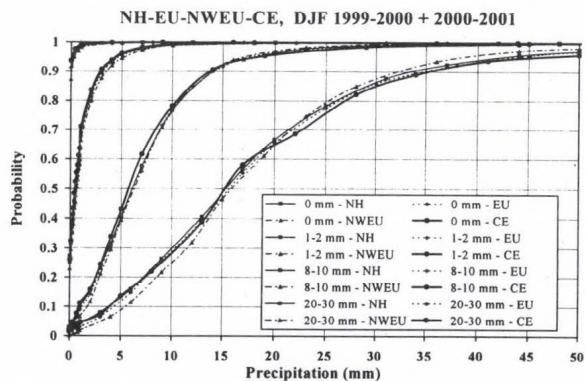
3. The new probability fields

For the generation of the new probability fields defined by Eq. (3), the precipitation thresholds of 1, 5, 10, 20, and 50 mm were defined. First the individual forecast values had to be transformed to probabilities for every threshold and season. These probability values can be easily determined from the PDF diagrams presented in *Fig. 3*. All we have to do is to read the frequency values of every curve (belonging to different forecast intervals) at a certain threshold. This is also highlighted in *Fig. 3* with vertical lines marking the thresholds. The required values are the crossing points of these lines and the PDF curves. Originally the cumulative functions show the probability of the observation below the threshold, thus a subtraction has to be done from 1. These frequencies concern the whole forecast intervals, thus we had to assign them an individual forecast value. The middle value of the forecast bins had been chosen. Finally, to get the desired probabilities for a precipitation forecast, we undertook a linear interpolation between the assigned discrete points. This simple method seemed to be sufficient enough even for higher forecasts, where the density of the function points are small.

To determine the seasonal relationship between forecast values and probabilities, the PDF sets of winter 1999–2000 and spring, summer, and autumn of year 2000 were taken. For the forecast intervals above 30 mm, the data sets of two years were combined to have sufficiently large sample sizes (2000+2001 for MAM and JJA, 1999+2000 for SON, and 1999-2000+

2000–2001 for DJF). The transform curves for every season and threshold can be seen in *Fig. 13*. The curves were not smoothed, so occasional jumps may be present.
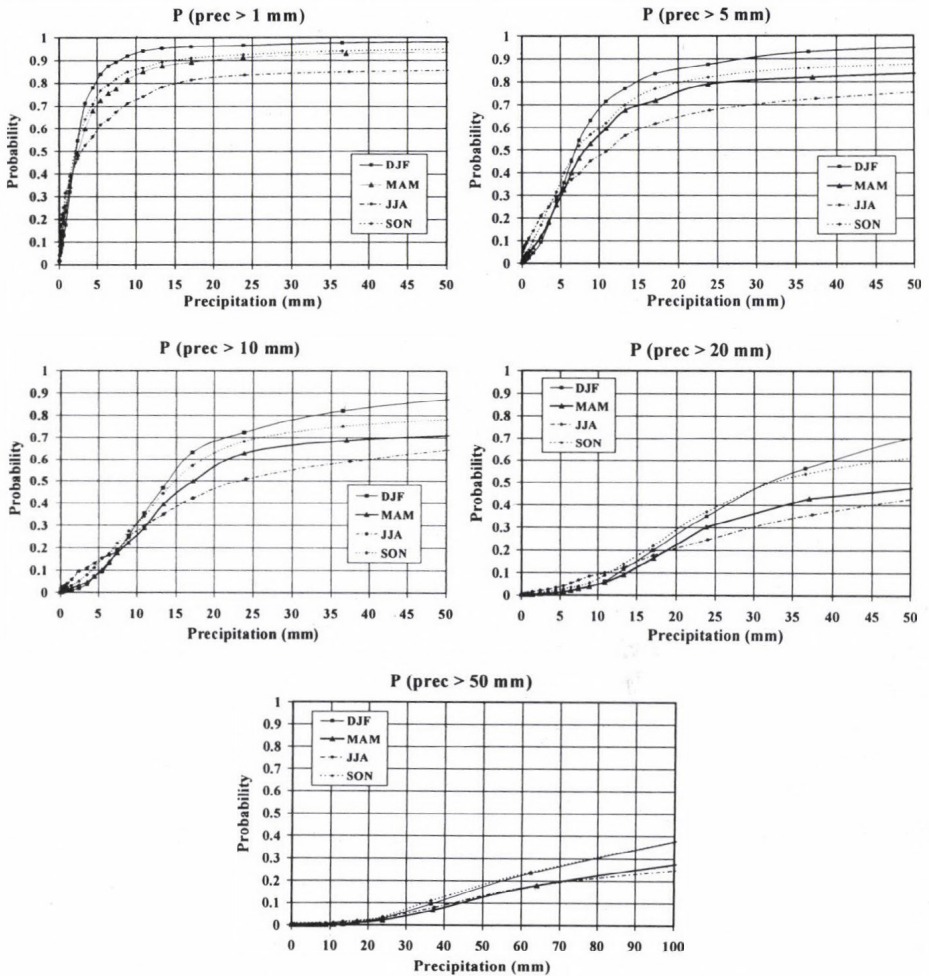
Fig. 13. Functions of the transformat.on of forecast values to probabilities for the thresholds of 1, 5, 10, and 50 mm.

During the experiments, probability fields were generated for all four seasons from September 2000 until August 2001. An example of the two probability fields is shown in *Fig. 14*. On the new forecast map the probabilities are spread further than on the old fields, and the maximum of the probabilities over wet regions is significantly lower with the new method.

These new features can be highlighted by two simple examples, when all members predict exactly 4 mm and secondly when 6 mm (the averaging of the 50 members contribution does not have any effect now). Let us consider the threshold of 5 mm. Now the operationally calculated probabilities differ sharply, namely in the first case we got 0%, and in the second case 100%. The new procedure distinguishes continuously between forecast values, and thus we have a same order of probabilities for these two cases. Moreover there is a chance of 5 mm rain even for the case when no rain was forecasted at all. For example, in the PDFs for autumn the probability of 4 mm is 28%, and for 6 mm it is 43%. With the new method there is an overall tendency of increasing the operational probability values around their minimum, while decreasing around the maximum.

Old probability – 5 mm   **New probability – 5 mm**
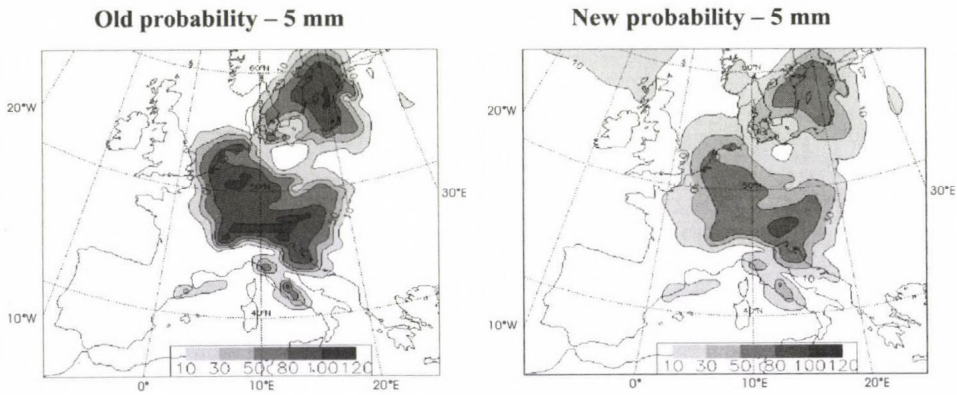
Fig. 14. Comparison of the probability fields (24 h PoP) created by the traditional democratic voting method (left), and by the new procedure (right), forecast of September 3, 2001, valid for: D+2, threshold: 5 mm.

4. Verification of experimental runs

We wanted to test the quality of this new type of PoP from as many aspects as possible. First, the probability fields for every full seasonal period had to be produced. We chose the seasons starting with SON 2000, and ending up with JJA 2001. Both the operational probabilities and our newly constructed probabilities had to be derived. The timing was chosen according to the users' needs, so we decided to prepare the probability fields for 06–06 UTC (24 hours period) consecutively for each day. Our target intervals thus have been selected as the following forecast ranges: 18–42 h, 42–66 h, 66–90 h, 90–114 h, 114–138 h, 138–162 h, 162–186 h, 186–210 h, 210–234 h (denoted from the forecasters point of view as D+1, D+2, ..., D+9).

As verification area, Europe has been chosen, focusing on the region where we have the largest number of available observations (only data in GTS). For qualitative evaluation we have chosen the most frequently used scores regarding probability forecasts (for a comprehensive overview of the scores and for the exact definitions see *Stanski et al., 1989; Persson, 2001*):

- Brier score ($BrSc = BSrel - BSrsl + Uncertainty$),
- Brier score of the sample climate ($= Uncertainty$),
- Reliability ($BSrel$),
- Resolution ($BSrsl$),
- Brier skill score with respect to the sample climate
  ($BCBrSkSc = 1 - \dfrac{BrSc}{SCBrSc}$),
- Brier reliability skill score ($BSSrel = 1 - \dfrac{BSrel}{SCBrSc}$),
- Brier resolution skill score ($BSSrsl = \dfrac{BSrsl}{Uncertainty}$),
- Relative operating characteristics (ROC).

We mainly present results for DJF and JJA, but the results for the other two seasons are very similar. Our primary interests were the reliability tables, ROC, and time series of Brier skill score with respect to sample climate and also time series of Brier resolution skill score.

Some results for JJA 2001 can be seen in *Fig. 15*. With the application of the new method, the operational overforecasting tendency turned to underforecasting for this summer period. The two pairs of curves are almost symmetrical to the diagonal line. Having analyzed the whole range of forecast steps and thresholds, we can summarize that the reliability is significantly better with the new probabilities for 1 mm. However, for bigger thresholds this is only true for D+1, afterwards there is no characteristic signal. The above stated underforecasting feature for probabilities greater than 20% is stronger for higher thresholds. It can also be seen from the figures, that the maximum of the predicted probabilities are significantly less for the new method than it was for the operational forecasts. This is just another evidence supporting our result with reference to the example of the two probability fields, as showed above.

Significant improvement in Brier skill score can only be seen for 1 mm, while for higher thresholds there is rapidly decreasing increment. In general the biggest difference can be detected for D+1. In resolution there is no significant improvement, but also there is no deterioration. If there is any increment it is only detectable during the first one or two days.
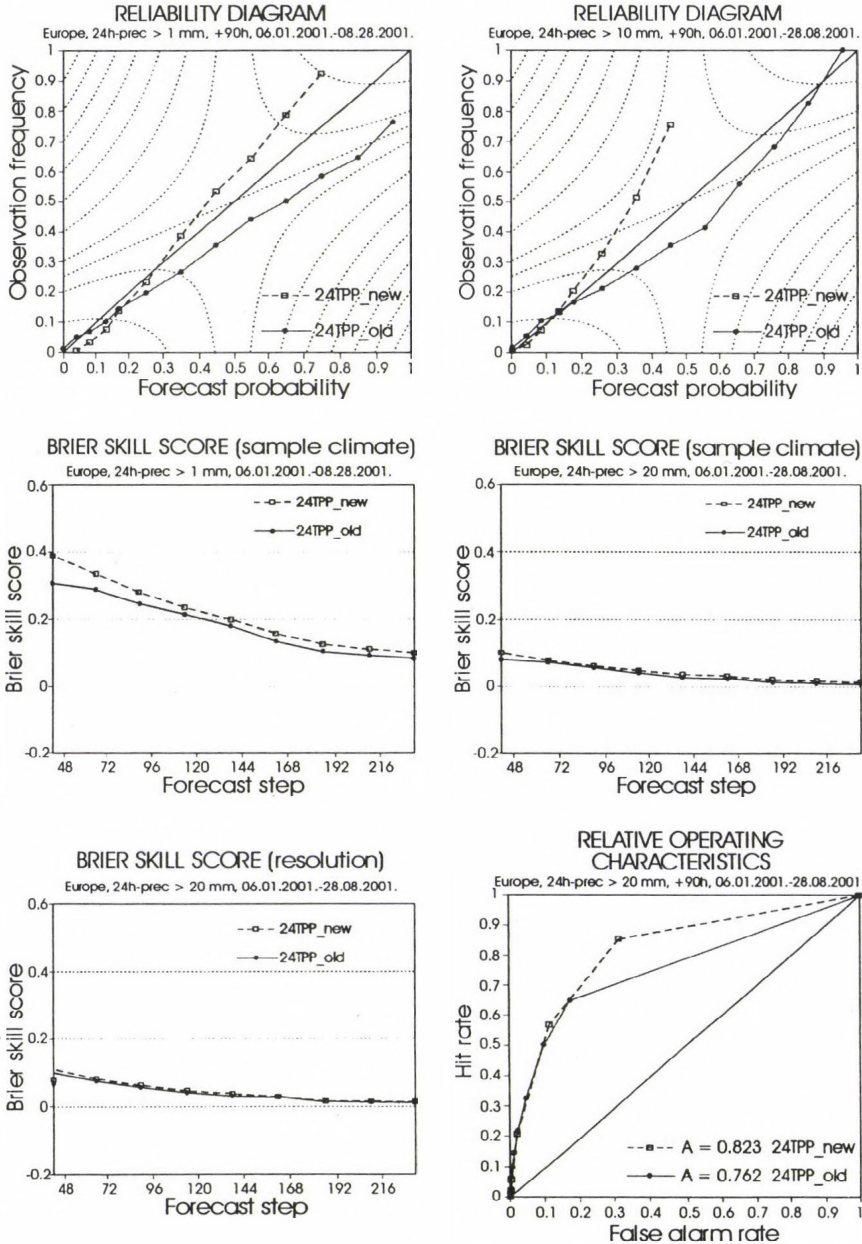
Fig. 15. A few verification diagrams for JJA 2001: reliability diagrams (first row; left: D+2, 1 mm; right: D+2, 10 mm), time series of Brier Skill Score with respect to sample climate (middle row; left: 1 mm; right: 10 mm), time series of Brier resolution skill score (3rd row; left: 20 mm), ROC (3-rd row; right: D+2, 20 mm).

For ROC curves the area under the curves, is the same for 1 mm, but there is greater improvement for higher thresholds, which is better emphasized for short range. The improvement is due to the higher hit rates gained with the new method.

As can be seen in *Fig. 16*, much better results were attained for winter. In general larger increments could have been obtained than for summer. The reliability is very good with the new probabilities, especially for small thresholds. For 1 and 5 mm after D+4 we could see some underconfidence, no significance bias for 10 mm, while for 20 mm and 50 mm there is overconfidence similarly to summer but with less magnitude.

The difference between the maximum of the forecasted probability values for a certain threshold and time step we had for summer is smaller here. The reason for this is the significant variability over seasons, as winter and summer are the opposite extremes (summer with lower, winter with higher frequencies), as we have already seen it in *Fig. 5*. In Brier skill score quite massive increment can be seen. For higher thresholds the difference decreases quickly again. With bigger time steps the curves are relatively closer to each other. In resolution there is slightly bigger difference compared to summer case, but still these increments, presented mainly for short range, are not significant. For ROC curves, very similar conclusions could be stated as we did for summer. The difference is just that we have some improvement here for 1 mm, for the first 1–2 days as well, and that for every other thresholds the increments are enhanced, and the differences in terms of ROC areas are more emphasized.

Regarding the season of MAM 2001, every aspect of the verification is impressively similar to JJA 2001: only a slightly larger overall improvements could be detected for spring (not shown). The results of the two other seasons, SON 2000 and DJF 2000–2001 are also similar to each other. In autumn the new probability fields deliver slightly smaller improvement over the operational probabilities, than it was for DJF. Increments for reliability are moderately smaller for SON, and the overforecasting tendency for 1 and 5 mm after D+4 is less emphasized.

Earlier we have shown some comparisons regarding the PDF curves for different accumulation periods of the forecasts, tested in JJA 2001. As we can see in *Fig. 17*, the best results were achieved with the forecast range of 06–30 h. The probability forecasts lost skill in every aspects of the verification consistently, as the lead time got longer and longer.

As an interesting aspect of this new PoP generation procedure, the variability of the forecast quality with respect to utilization of different years PDF set has also been tested. The summer period have been chosen again, during 1999 and 2000, where the PDF curves differed significantly.
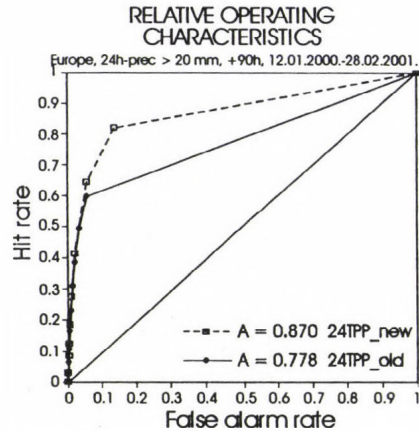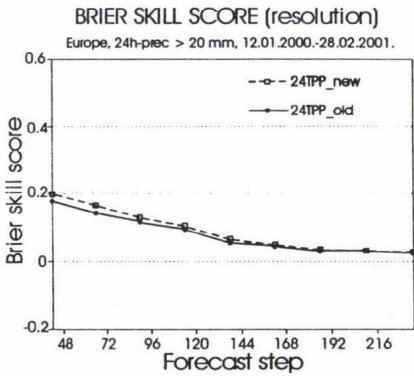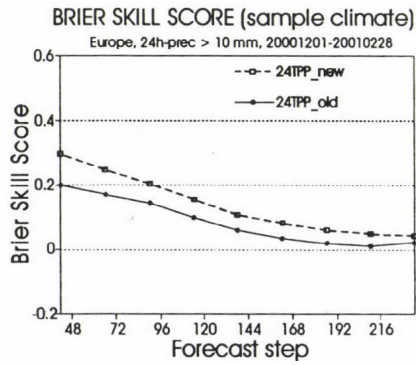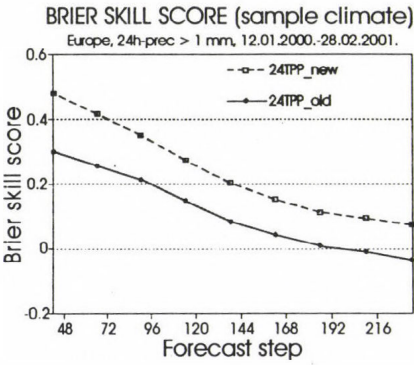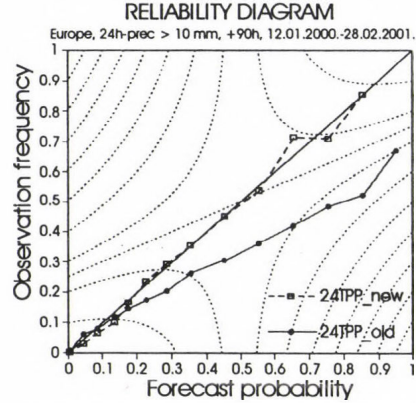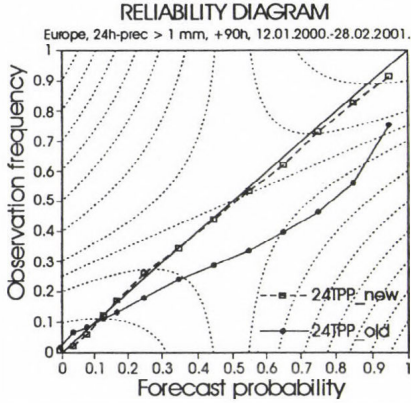
Fig. 16. A few verification diagrams for DJF 2000–2001: reliability diagrams (first row; left: D+2, 1 mm; right: D+2, 10 mm), time series of Brier skill score with respect to sample climate (middle row; left: 1 mm; right: 10 mm), time series of Brier resolution skill score (3rd row; left: 20 mm), ROC (3-rd row; right: D+2, 20 mm).

According to *Fig. 18*, moderate but systematic difference can be found between the quality performance of the two PDF sets. For resolution and ROC curves the results were almost identical, while there is slight and constant deterioration in Brier skill score and reliability for every threshold and time step. On the reliability diagram some shifts towards under-forecasting can also be seen, relative to the curve of 06–30 h. This is probably caused by the smaller frequencies of occurrence in the 1999's PDF sets (see *Figs. 6–9*).
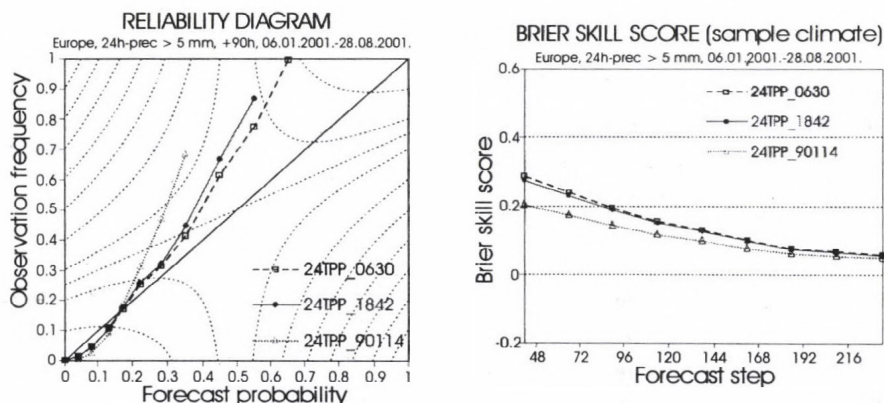
Fig. 17. Two examples of the comparisons between verification results of new probability fields, calculated by PDF-s of the forecast interval 06–30 h, 18–42 h and 90–114 h, verification period is JJA 2001.
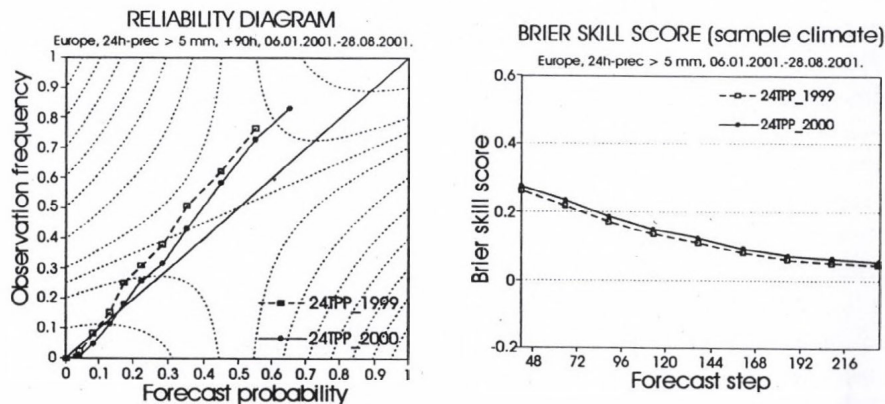
Fig. 18. Two examples of the comparisons between verification results of new probability fields, calculated by PDF-s of JJA 1999 and 2000, verification period is JJA 2001.

5. Summary, conclusions

In this paper we presented and tested a new and complex method for downscaling precipitation probabilities. Our basic idea – to calibrate the ensemble forecasts with conditional probability distributions of the forecasts-observation space – has produced promising results.

The generation of the probability distribution functions (PDF) was the first step in order to create the new probability fields. The PDFs were derived consistently for 22 different forecast intervals, for the forecast range of 06–30 h (24 hours period). Because of sample size requirements, the area of Northern Extra tropics was chosen, and the statistical analyses were performed for three months (seasonal) periods. Only a very small difference between two or three years seasonal PDFs could have been found, as long as the model environment was consistent. In addition, the geographical variability was also tested, without being able to demonstrate significant differences between smaller areas – like Central Europe. Thus, the geographical choice of the whole Northern Extra tropics seemed to be appropriate to be the basis for the statistical creation of the new probabilities for areas with significantly different climate.

The new fields that were calculated with probabilities for the local scale looked quite differently, in comparison with the operational probabilities. Because of the statistical calibration, the new fields are much smoother, the wet areas are spread out, and meanwhile the maximum value of the new probabilities is usually significantly smaller.

For testing the seasonal quality of the forecast, the new probability fields have been verified for different seasons (SON 2000, DJF 2000–2001, MAM 2001, and JJA 2001). The new method, in general, delivered better results than the operational one. The best results could have been obtained for winter, while the least improvement was attained for summer. While the old probabilities were underconfident for most of the cases, the new probabilities showed some overconfidency. In general, there is no significant improvement in the resolution, but as an important result there is no deterioration at all. The greatest improvement was gained for the Brier skill score, especially for the thresholds of 1 mm and 5 mm. Concerning ROC curves, some improvements (higher hit rates) were also present, mainly for bigger thresholds. Strong similarities were found between the results for JJA and MAM, and also in the case of DJF and SON, which can probably be explained by local scale convection.

In the future we would like to make verification with data from other years, as well. Preparing the PDFs using Control forecast data (EPS run starting from the deterministic model's initial state) instead of the T319 operational run, the model inconsistencies between the EPS forecasts, and the

statistically investigated forecasts could be eliminated. We also are planning to verify this new method of downscaling with very high density observational network.

References

Ehrendorfer, M., 1997: Predicting the uncertainty of numerical weather forecasts: A review. *Meteorol. Z. 6*, 147-183.

Ghelli, A. and *Lalaurette, F.*, 2000: Verifying precipitation forecasts using upscaled observations. *ECMWF Newsletter*, No. 87 [Available from ECMWF, Reading, England].

Hamill, T. M., 2001: Interpretation of Rank Histograms for Verifying Ensemble Forecasts. *Mon. Weather Rev. 129*, 550–560.

Palmer, T.N., Molteni, F., Mureau, R., Buizza, R., Chapelet, P., and *Tribbia, J.*, 1992: Ensemble prediction. *ECMWF Research Department Tech. Memo.* No. 188 [Available from ECMWF, Reading, England].

Persson, A., 2001: User Guide to ECMWF forecast products. [Available from ECMWF, Reading, England].

Stanski, H.R., Wilson, L.J., and *Burrows, W.R.*, 1989: Survey of common verification methods in meteorology. *World Weather Watch, Technical Report* No. 8, WMO/TD. No. 358.

General characterization of the lightnings in the Carpathian Basin

Ferenc Wantuch[1*] and **Sándor Szonda**[2]

[1]*Hungarian Meteorological Service,*
P.O. Box 38, H-1525 Budapest, Hungary; E-mail: wantuch.f@met.hu

[2]*Hungarian Power Companies Ltd,*
P.O. Box 15, H-1255 Budapest, Hungary; E-mail: sszonda@vmv.hu

Abstract—The paper is a review of the general features of lightning records produced by the System d'Alerte Foudre par Interferometrie Radio-electrique (SAFIR) lightning detection system used in Hungary over the recent 5 years. The intra-cloud (IC) and cloud-to-ground (CG) lightnings were distinguished. Lots of information was generated with the help of this system. The electrical parameters were collected and processed. The time and spatial distributions of the lightnings and different type of lightning characteristics were computed. As the first discharges appear in the early time of the forming of a cumulonimbus cloud, the application of data generated by the lightning detection system is a good tool in the every day meteorological short range forecasting. Understanding of the lightning physics leads to the more effective meteorological and industrial application.

Key-words: SAFIR lightning detection system, interferometria, intra-cloud, cloud-to-ground, electrical parameters

1. Introduction

Thunderstorms are composed of convective cells developed due to the thermal instability of moist air. These cells usually fasten the growth process of each other. The horizontal size of thunderstorms can be of several tens of kilometers, while their lifetime can reach several hours. Convective cells are developing very fast, they can reach the height of 10 km in just several tens of

---

* Corresponding author

minutes. A strong updraft is present in the developing phase of the cells, which carries up ice crystals, overcooled water drops, and snowflakes. The basic processes of the loading of thunderclouds with electricity are the charge separation for both water drops and ice crystals and the separation of oppositely charged particles due to the irregular updraft. Usually, a triple electric pole develops inside the thundercloud as a result of these processes: a large negatively charged zone in a height of about 6 km, a positive zone at 8–12 km, and a weak positive layer at the cloud base level. A weaker electric field develops at the lower parts of the cloud, while in the upper part the electric field strength is several 100 kV/m. The time necessary for electric charge for one cell is less then tan minutes.

A very complicated process takes place as soon as the electric field strength reaches the air's capacity of electrical penetration. First, charges are concentrated by short jumps of several hundred meters and halts of several dozens of µs, and the air becomes pre-ionized along the jump paths. On the ground, charges with opposite polarity are gathering due to the big field strength produced by the approaching charges and good electric conductance of the ground, and they are moving upwards forming a counter discharge. When the two oppositely directed channels meet, the main discharge of the lightning forms. The whole process takes several hundred milliseconds, while the lightning itself takes only several tens of µs. Lightning is a self-destructive process, because the lightning channel is continuously narrowing due to the electric fields caused by the lightning current, and it breaks eventually. If all charges were not neutralized till the breaking of the channel, then new and new lightnings may occur with several hundred ms of delay (multiple lightning) in the previous channel, which still remains ionized after the discharge.

The process mentioned above is accompanied by electromagnetic radiation on a broad frequency spectrum, which is radiated out by the lightning channel as if it were a huge antenna. The frequency spectrum ranges from several kHz to 1–2 GHz. The dynamics of the movement of electric charges and, therefore, the spectra of the produced radiation differs significantly if the lightning occurred inside the cloud or if it has reached the ground. This gives us the possibility of distinguishing the cloud lightnings from the cloud-to-ground lightnings.

2. Installing the lightning detection system

The high-frequency VHF radiation of lightnings offers the possibility of observing the thunderstorm activity. The SAFIR lightning detection and forecasting system used in Hungary was developed by a French office,

ONERA (Office National d'Etudes et de Recherches Aérospatiales), for warning purposes of the rocket launching pad in French Guyana against thunder stroke (*Larosche et al.,* 1991). The system was produced for civil application purposes by the firm Vaisala-Dimension.

The SAFIR system is able to determine the position of lightning with an accuracy of several kilometers based on interferometrial direction measurement. The direction measurement is based on the dislocation of phase between the electromagnetic waves reaching the four or eight closely mounted dipole antennas belonging to the sensor unit. The accuracy of the measurement depends on the number of antennas. The Hungarian system consists of five dipole antennas. The chosen frequency range for observation is 108–118 MHz. The high sensitivity of the system makes possible the detection of the low energy cloud-to-cloud lightnings, which can warn the user several 10 minutes before the first lightning reaches the ground. Let us see an example. *Fig. 1* shows the changes in the numbers of cloud and ground lightnings registered on August 1, 1999 with a 5-minute integration time. During this afternoon thunderstorm the cloud lightnings began 30 s earlier and ended 45 s later than the ground lightnings.
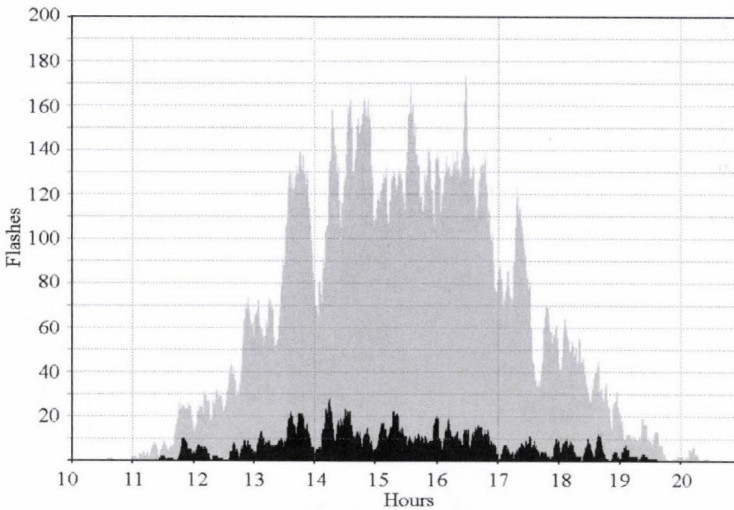

Fig. 1. IC (grey) and CG (black) lightnings registered on August 1, 1999 with a 5-minute integration time over Hungary.

The SAFIR system also has a low frequency (0.3–3 MHz) antenna, which is able to detect the strength of the produced electric field and the shape of the indication of lightnings. Based on these measurements it is possible to define

113

whether the lightning has reached the ground. With the use of propagation models, the following lightning parameters can also be derived:
- peak current (kA),
- rise time (μs),
- decay time (μs),
- steepness (kA/μs),
- polarity,
- electric charge (As),
- the energy of the impulse (kA2s).

The sensors of the SAFIR system have a GPS based synchronizing time of 100 ns, and they are able of doing a localization every 100 μs. The centre and the sensors are in continuous touch – they are sending data in every second, so the system can follow the events in real-time mode.

The intention of installing a lightning detection system for Hungary first occurred in 1995. After a long period of preparation and organization, the establishment of the system began in 1997 using the elements of the SAFIR system as an investment of the Hungarian Meteorological Service. As a first step, three stations were established (Budapest (later moved to Bugyi), Sárvár, and Véménd) which provided a 60% coverage of the country. In 1998 two more stations were added (Zsadány and Várboc). Finally, in September 1998 the system was replaced by the newly developed product of Vaisala-Dimension, which had an entirely digital data processing system, and additional sensors were installed, which are able to measure the electric characteristics of lightnings. Due to the strict requirements, like horizon limitation, a spectrum with low background noise, available communication lines, power supply, etc., the sensors were mounted on the high communication towers of the T-Mobile Phone Ltd. The area under continuous observation is about 200,000 km^2 with the detection criteria set by the Vaisala-Dimension, and it also covers some parts of the neighboring countries. The system can localize the lightning with an accuracy of 1–2 km over Hungary, the probability of detection is above 98% (*Richard,* 1998). Both the accuracy of location measurement and the probability of detection decrease towards the limits of the area under observation.

The system can distinguish the ground strokes from cloud lightnings based on the following parameters:
- rise time: 0.125–15.0 μs,
- decay time 15–255 μs,
- peak current intensity: minimum 3 kA,
- detected electric field strength: minimum 1 V/m,
- time coherence: 200 ns,
- number of detecting stations: 3 – sometimes 2.

If these criteria are satisfied simultaneously, then the system assumes that the lightning is a groundstroke. Further statistical analyses are dealing only with these groundstrokes.

3. Evaluation of lightning data registered in 1999–2003

The observational network worked continuously, but in 2002 the SAFIR system was out of work by technical reasons. Thus 4 years of lightning database was collected. The system has registered 3,920,083 lightnings over the whole territory. The summarized lightning distribution – calculated for cells of 5×5 km – can be seen in *Fig. 2*. It happened several times that a station was out of work for shorter or longer time periods. The effect of this can easily be recognized in the cigar shaped NW-SE directed stripe between Sárvár and Véménd. Sárvár is located in the western, while Véménd is located in the south-western part of Hungary.
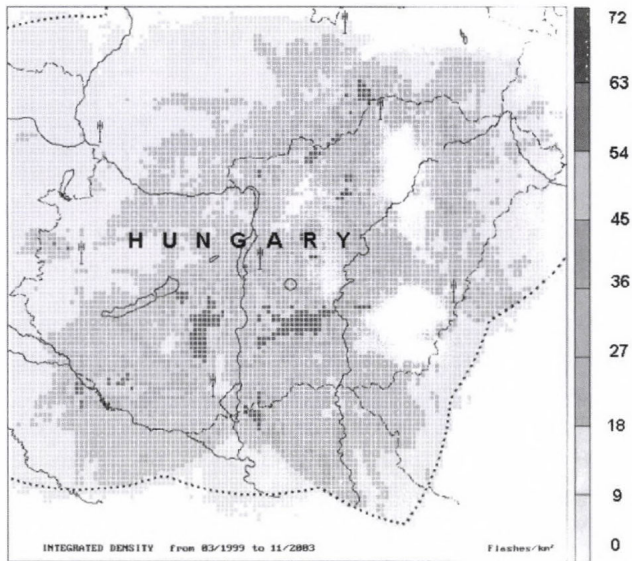
Fig. 2. CG and IC lightnings (flashes/km^2) in the time period of 1999–2003 (except 2002).

The most frequent occurrence of cloud lightnings consists of three parts. First one was observed at the central part of Hungary, the second is in the southern part of Mátra Mountains next to the northern border. Third one is located near the SW border.

The examined 4 years are too short to establish any climatological features, but in the future we can generalize a very detailed new lightning climatological database of Hungary. Such database would be very useful for the industrial lightning protection.

After the spatial occurence, the time distribution was generalized for the mentioned years. Two maximum were observed, the first in afternoon, the second in nighttime. Less lightning was observed in the morning time (*Fig. 3*). These results are harmonized with earlier climatological maps.
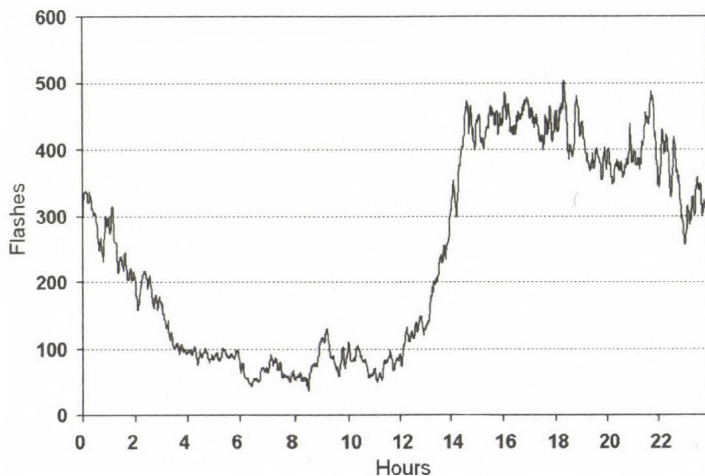
Fig. 3. Average number of CG lightnings in 5-minute over Hungary in 1999–2003 (except 2002).

Fig. 4 illustrates the composite picture of SAFIR data and radar echo. The idea was based on *Sonoi et al.* (1999). This visualization and comparison have two advantages. A larger part of bad observations, caused by interference and background noise, was filtered. On the other hand, the forecaster can distinguish electrical active part of cumulonimbus from the territories represented by intensive precipitation and radar signal. The IC lightning is a very good marker to find developing thunderstorm cells. The shape of active thunderstorm cell is well defined with the IC lightnings (*Weber et al.,* 1998).

The first IC discharges appear in the early time of the forming of a cumulonimbus cloud. The application of observed data generated by the lightning detection system is a good tool in the short range forecasting (*Kononov et al.*, 2000). The rate of CG and IC lightning in the whole data set is about 10% (*Fig. 5*). It means that from a statistical point of view ~1 CG lightning/km²/year is a good estimation for Hungary.

116
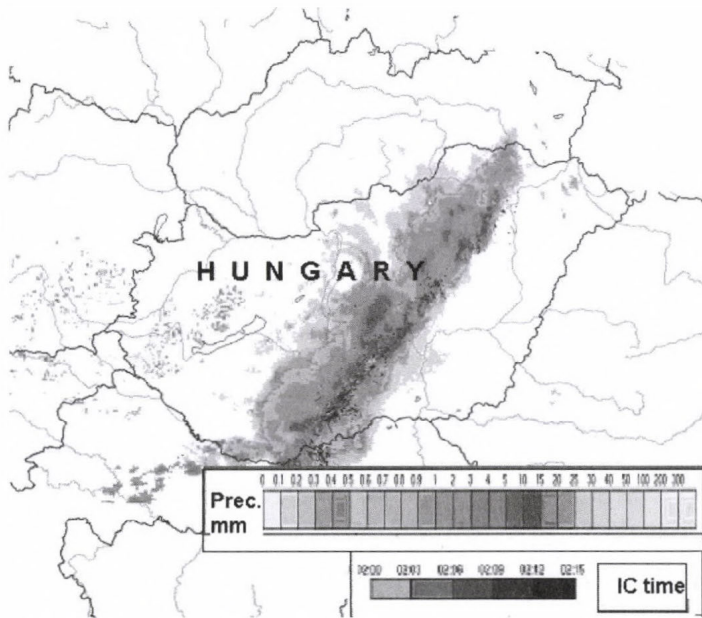
Fig. 4. Combined SAFIR and radar observation visualization on August 30, 2003, 02:00–02:15 UTC.
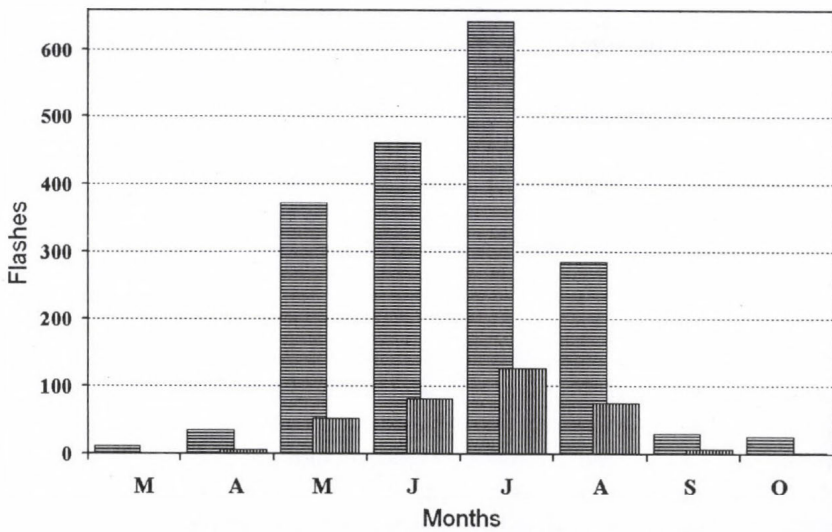
Fig. 5. Monthly IC and CG distribution in 1999–2003 (except 2002)
(IC is striped horizontally, CG is striped vertically).

3.1 Polarity

The next electrical parameters are based on the 349,609 CG lightnings registered on the territory of Hungary in 1999–2003. Most of the lightnings (90%) had a negative polarity (*Fig. 6*). This fact is well known from other studies (*Szonda* and *Wantuch*, 2001). The negative lightnings belong to the individual convective process in the atmosphere. The registered database shows that the ratio of positive lightnings decreases during summer. The positive lightnings belong to the weather frontal effects with probably large ice crystals. In wintertime the positive lightnings are the dominant ones.
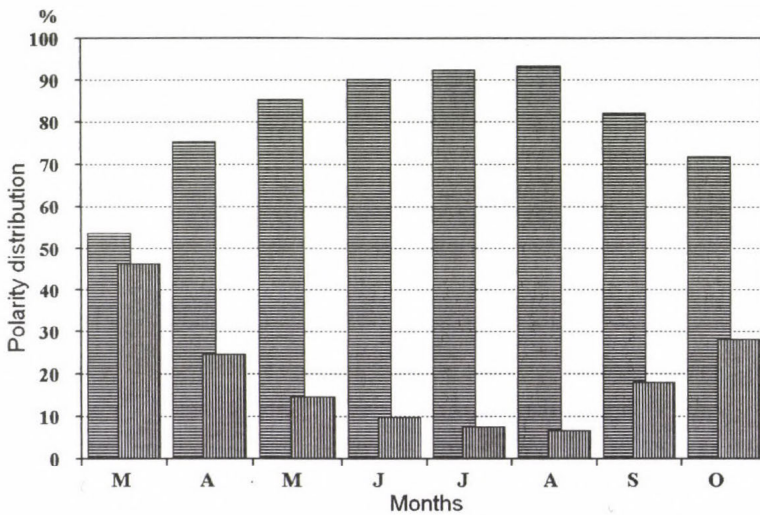
Fig. 6. Monthly current polarity distribution in 1999–2003
(negative polarity is striped horizontally, positive polarity is striped vertically).

3.2 Multiple lightnings

The system assumes that different lightnings belong to a multiple lightning if they occur at the same place or in a predefined distance (5 km) and time sequence (0.5 s). The statistical analysis shows that 79,6% of the positive lightnings are single, and 60.6% of negative lightnings are single. In case of double lightnings this effect is turned. It is in accordance with the result of scientific literature. So, negative discharges are more likely to produce multiple lightnings. The distribution of the positive, negative, and the total multiple lightnings of 1–6 strokes is presented in *Fig. 7*.
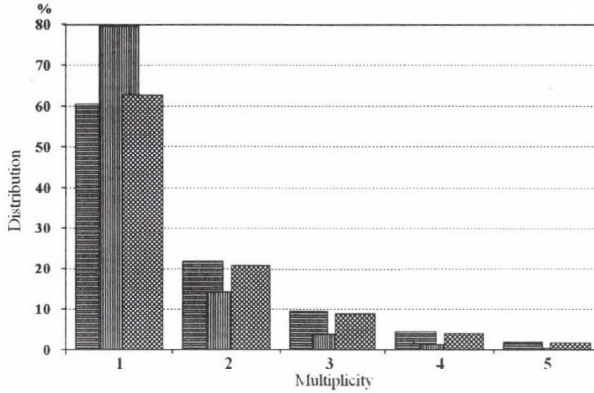
Fig. 7. Probability of multiple lightnings (negative lightnings are striped horizontally, positive lightnings are striped vertically, total lightnings are dotted striped).

3.3 Peak current

The peak current intensity (kA) can be calculated from the strength of the electric field (V/m) at the antenna location and the distance (m) of the lightning. In the next figure (*Fig. 8*), the characteristic distribution function of positive (+) and negative (–) lightnings is presented together with the number of lightnings in each discrete current intensity interval. One can observe a significant difference between the current intensities of the lightnings with different polarity. The average value for positive lightnings is ~25 kA, while for negative lightnings it is ~38 kA. On the other hand there are more positive lightnings which are stronger than ~70 kA. The largest registered values were +623 kA and –590 kA.
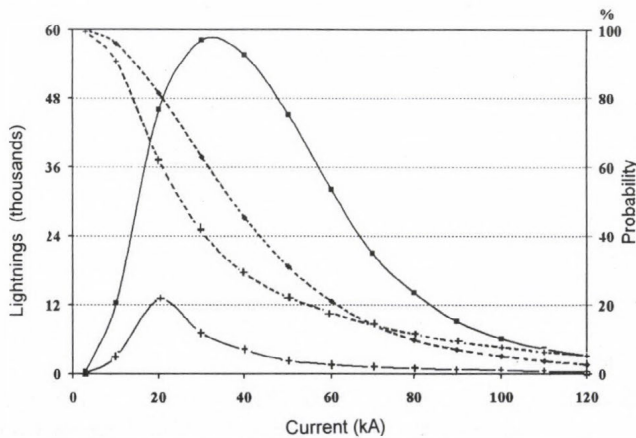
Fig. 8. Distribution of peak current.

3.4 Rise time

Measuring of the rise time with the SAFIR system (*Fig. 9*) is possible between 0.125 and 16.0 µs. The lowest registered value is 0.3 µs, the most frequent value is 6.2 µs. The average value is ~7.2 µs.
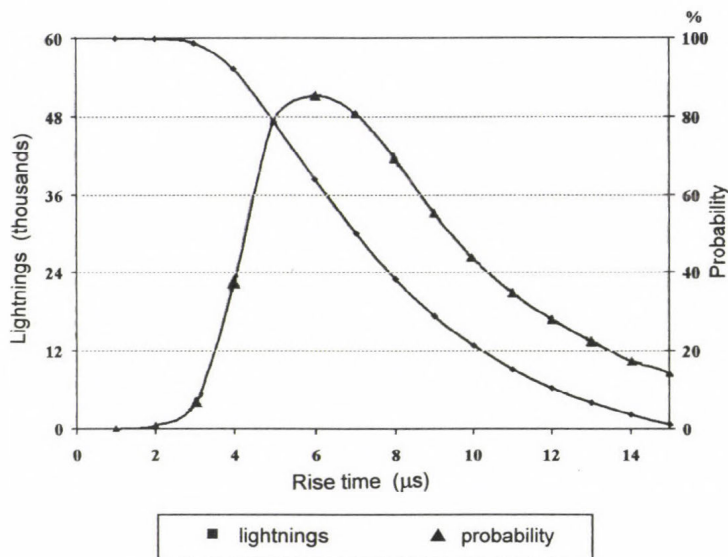
Fig. 9. Distribution of rise time.

3.5 Decay time

Unusually, instead of the half time, the system gives the so-called decay time (that is the time between the peak value and the lower limit of 3 kA). The measuring range for this parameter is set for 16–255 µs. The average value is ~28 µs, the most frequent value is 25 µs. The distribution curve looks much more equalized than in the case of rise time.

3.6 Steepness of rising phase

The very interesting value of current steepness from electrotechnical point of view can be calculated from the current intensity and rise time. The lowest steepness determined by the predefined limit values (3 kA and 15 µs) is 0.2 kA/µs, the lowest registered value for both negative and positive lightnings is 0.5 kA/µs. The maximum steepness differs for the differently polarized

120

discharges: for positive lightnings it is 509 kA/μs, while for negatives it is less than half of it: 237 kA/μs. These values are very large for the 90% of front steepness values, which are below 13 kA/μs.

3.7 Electric charge

The charge of lightnings can be calculated from the rise time, decay time, and peak current values. The predefined lower limit (0.125/15 μs and 3 kA) allows the calculation of the lowest charge beginning with 56×10^{-9} As. The lowest registered value is many times larger than this, it is 0.068 As. There is a significant difference between the charge of the positive and negative lightnings. The average value for positive lightnings is ~0.5 As, for negative lightnings it is much larger: ~0.7 As. There is almost no difference between the maximum charge values, for positive lightnings it is 37 As, for negatives it is 39 As. These values are extremely high, because 90% of charge values are below 1.8 As.

3.8 The energy of the impulse

The integration of the current square – time values gives a number that is proportional to the energy content of the lightning. Similar to the charge, the lower limit determined by the predefined parameters is small. The lowest registered value is 0.00029 kA^2 s, the largest is 10.55 kA^2 s. The distribution function on the next figure shows that the average value is only 0.02 kA^2 s, and the 90% of the values are below 0.06 kA^2 s.

It can be said that the first test years of the Hungarian lightning detection system were successful. Registered data meet the historical data from literature both in the case of the number of lightnings and the lightning parameters.

4. Conclusion

In 1999, the installation of a lightning detection system was completed in Hungary. This system is suitable not only for detecting and registering intra cloud (IC) and cloud-to-ground (CG) discharges, but it is also capable of identifying major lightning parameters in case of the latter. This paper introduces the SAFIR system, and also includes the most significant statistical data on discharges registered during 1999–2004. The observed information is useful for everyday meteorological work and industrial application.

References

Kononov, I.I., Petrenko, I., and *Yusupov, I.E.,* 2000: Space-temporal variations of electromagnetic radiation of thunderstorms in the process of their evolution. *25th International Conference on Lightning Protection.* Sept 18, 2000, Rhodos, Greece.

Laroche, P., Malherbe, C., Bondiou, A., Weber, M., Engholm, C., and *Coel, V.,* 1991: Lightning activity in microburst producing storm cells. *25th International Conference on Radar Meteorology.* June 1991, Paris, France.

Richard, P., 1998: Propositions of methods of validation of lightning localisation systems performances. *International Conference on Lightning Protection.* September 1998, Birmingham, U.K.

Sonoi, Y., Kawasaky, Z.I., Maekawa, Y., Fukao, S., and *Takashi, T.,* 1999: Observations of thunderclouds and lightning activity in winter by dual polarization radar and SAFIR. *11th International Conference on Atmospheric Electricity.* June 7-11,1999, Guntersville, Alabama.

Szonda, S. and *Wantuch, F.,* 2001: Examination of lightnings detected by SAFIR system in 1999 (in Hungarian). *Elektrotechnika 94,* No. 2, 54-57.

Weber, M.E., Willliams, E.R., and *Wolfson, M.M, -Group 43-, Goodman, S.J.,* 1998: An assessment of the operational utility of GOES lightning mapping sensor. NASA/Marshall Space Flight Center. *Project Report NOAA-18.*

A study of ultraviolet solar radiation at Cairo urban area, Egypt

S. M. Robaa

Astronomy and Meteorology Department, Faculty of Science, Cairo University,
P.O. Box 12613, Giza, Egypt; E-mail: d_robaa@hotmail.com

Abstract—Monthly mean daily values of global (G) and ultraviolet (UV) solar radiation incident upon a horizontal surface at Cairo urban area during two different periods (1969–1973 and 1993–1997) are presented, analyzed, and compared. The effect of urbanization processes on the solar radiation components is investigated and discussed. It was found that the total amount of the two radiation components, G and UV, received at the urban area of Cairo during the period 1969–1973 highly exceeds the total amount received during the period 1993–1997 for all months of the year. The mean relative reduction of G and UV reached 17.4% and 27.4%, respectively. A significant correlation between G and UV radiation has been found, and the recommended correlation equation has been stated to estimate the values of UV radiation which is difficult to measure at any site in the zone of Lower Egypt. Also, a comparative study of the two radiation components, G and UV, at urban (Cairo) and rural (Bahtim) areas during the period 1993–1997 revealed, that the urban area always has values of G and UV radiation distinctly lower than values found in rural area for all months of the year. Urban-rural mean reduction of G and UV reached 7.0% and 17.9%, respectively. The ratio of the ultraviolet to global radiation (UV/G) are calculated and compared with other sites in the Arabian Peninsula. The effect of atmospheric dust on the measured solar radiation components is also investigated and discussed.

Key-words: urbanization, industrialization, atmospheric dust, ultraviolet solar radiation, global solar radiation, urban areas, rural areas

1. Introduction

Ultraviolet solar radiation either at the edge of the atmosphere or at the Earth's surface, accounts for only a small fraction of the total radiation flux. In outer space, UV radiation accounts for only about 8.73% of the total solar radiation (*Al-Aruri et al.,* 1988), while at any location on the Earth's surface, the UV

radiation value depends on solar zenith angle, atmospheric ozone content, and transparency of the atmosphere (*Kylling et al.*, 2000; *Kirchhoff et al.*, 2002; *Luccini et al.*, 2003). UV radiation wavelength range has been divided into three sub-ranges; UV-A (400–315 nm), UV-B (315–290 nm), and UV-C (290–220 nm). The mentioned lower limit of UV-C (220 nm) is valid only when it is studied in air, but in fact, the wavelength of the shortest wave ultraviolet beams is shorter than 100 nm. The earth surface receives only UV-A and UV-B, while the UV-C component is removed not only by absorption through the protective ozone layer (O_3) but also because it provides energy for several photoionization processes. UV-B is partially absorbed by the ozone layer, while UV-A is transmitted (*McKenzie et al.*, 1995). There are many beneficial and damaging effects of UV-A and UV-B radiation on humans, the ecosystem, animals, plants, and materials (*Parrish et al.*, 1978; *Biswas*, 1979; *Giese*, 1982). High doses of ultraviolet radiation, especially band B, causes skin diseases, eye cataract, photo-decomposition, degradation of materials, and may also harm crops (*Som*, 1992). Inverse relation is known between the ozone density in the atmosphere and the amount of UV reaching the Earth's surface. From this point of view, the UV radiation is highly affected by the ozone which is destroyed by pollutants such as freon refrigerants, spray, and atomic bomb tests (*Elhadidy et al.*, 1990; *Fiester* and *Grasnick*, 1992; *Tang et al.*, 1998; *Zerefos el al.*, 2001; *Wuttke et al.*, 2003).

In Egypt, measurements of UV radiation have been taken for last few years. Measurements of global solar radiation began in 1969 at both Cairo and Bahtim using an Eppley pyranometer (Model PSP). The ultraviolet radiation has been measured in Egypt since 1990 at only two meteorological stations of Cairo in the north and Aswan (23°58'N; 32°47'E) in the south, using an Eppley radiometer which is sensitive to radiation in the wavelength band 290–385 nm (*Salem*, 2000). Although the study of UV radiation is very important because of its dramatic biological effects on humans, animals, plants, the earth's surface, and surrounding atmosphere, the concerned studies of UV radiation is very rare in Egypt. Therefore, the main objective of this paper is to study the characteristics and behavior of UV radiation, and the impact of urbanization on its values at Cairo urban area.

2. Geography and description of the study area

In this study, two Egyptian meteorological stations, namely Bahtim and Cairo, have been selected to represent rural and urban areas, respectively. The two selected stations lie inside the greater Cairo region. Brief description of these two stations is given below.

1. Bahtim agrometeorological station (30°08'N; 31°15'E) lies about 13 km to the northwest of central Cairo near the border between urbanized and cultivated area. It has been established at the end of 1966 in the field of the Agricultural Research Station of the Agricultural Society at Bahtim and has been working on a routine basis up till now (2003). Bahtim area was dominated by vegetation and characterized by clearness of its atmosphere. The surrounding area was also cultivated land, and it was considered to be a good example of the rural area. Unfortunately, the population and human activities started to increase rapidly in Bahtim area during the last few years.

2. Cairo meteorological station (main building of the Egyptian Meteorological Authority) (30°05'N; 31°17'E) lies on the east bank of River Nile near central Cairo on the road leading from the city to the suburb of Heliopolis, to the northeast part of Cairo city. Much of factories exist in the near-by area also, where high density of buildings and population exists in addition to thousands cars and buses. Streets are covered by asphalt and gardens are not abundant. The local soil is originally desert sand. Generally, air quality in Cairo station represents the typical urbanization effects in and around Cairo City.

3. Results and discussion

3.1 Relationship between G and UV solar radiation

Because the measurements of UV radiation are not available at any location in Egypt, except of the two stations of Cairo and Aswan, the estimation of UV at the rural area of Bahtim is of real benefit, especially for the present study.

Clear linear correlation between the ultraviolet and global solar radiation has been found in many studies (*Fiester* and *Grasnick*, 1992; *Koronakis et al.*, 2002). Therefore, many types of correlations were tried to get out the best fit between G and UV radiation at Cairo using all available monthly mean values of the two parameters for nine years from 1990 to 1998. A significant positive correlation between G and UV radiation has been found in the form

$$UV = a\,G \pm b, \qquad (1)$$

where a and b are the regression coefficients depending on the weather parameters of the location. Data has been processed using an advanced computer program, and the obtained values of a and b were 0.0349 and 0.0261 for Cairo, which represents the typical weather conditions of Lower Egypt. The obtained values of the correlation coefficient is 0.98 and the standard error

of estimate is 0.0023 (*Fig. 1*). The deduced empirical relationship (Eq. (1)) becomes

$$UV = 0.0349\,G - 0.0261. \tag{2}$$
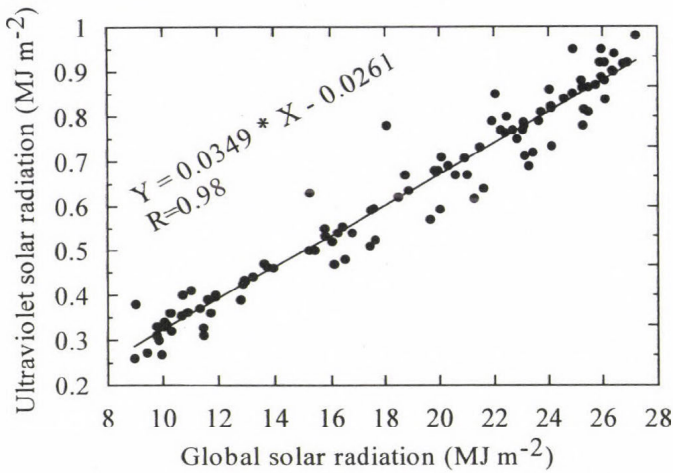
Fig. 1. Correlation between global and ultraviolet solar radiation at Cairo.

3.2 Verification of the empirical equation

To verify the deduced empirical equation (Eq. (2)), the monthly mean values of UV have been calculated for two years, 1999 and 2000, at Cairo using the corresponding values of the measured G radiation and applying Eq. (2). The estimated UV radiation was compared with the corresponding measured data during the same two years, 1999 and 2000. The results are listed in *Table 1*. It can be seen, that the estimated values of UV radiation are in a good agreement with the measured values for all months of the year. The percentage error was found ranged from –2.4 to +5.9, and from –3.7 to +5.1 during the two years, respectively, and from –3.0 to +5.2 for the average data of the two years. The annual mean values of the percentage error of the two years and their average values have been found +1.06, +1.27, and +1.16, respectively (see *Table 1*).

Therefore, it is concluded, that the empirical formula (Eq. (2)) could be used to make the determining of the UV radiation more precise at any location inside Lower Egypt, where there are no measured data of UV radiation or there are instrumental and other difficulties encountered in measuring of UV radiation.

Table 1. Comparison between the measured (UV_m; MJ m^{-2}), and estimated (UV_s; MJ m^{-2}) values of ultraviolet radiation, the percentage error of the estimated values (E%), and the measured global radiation (G_m; MJ m^{-2}) at Cairo during the two years of 1999 and 2000, and the average of the two years

Month	1999				2000				Average of the two years			
	G_m	UV_m	UV_s	E%	G_m	UV_m	UV_s	E%	G_m	UV_m	UV_s	E%
Jan	11.22	0.374	0.365	2.2	10.44	0.345	0.338	2.0	10.83	0.359	0.352	2.1
Feb	13.63	0.446	0.450	−0.8	14.56	0.483	0.482	0.2	14.10	0.465	0.466	−0.3
Mar	18.70	0.620	0.626	−1.0	19.13	0.624	0.642	−2.8	18.91	0.622	0.634	−1.9
Apr	22.89	0.814	0.773	5.1	23.80	0.848	0.805	5.1	23.34	0.831	0.789	5.1
May	25.71	0.926	0.871	5.9	26.02	0.923	0.882	4.4	25.86	0.924	0.877	5.2
Jun	27.44	0.962	0.932	3.1	27.12	0.959	0.920	4.0	27.28	0.960	0.926	3.5
Jul ·	26.52	0.936	0.899	3.9	26.48	0.927	0.898	3.1	26.50	0.931	0.899	3.5
Aug	23.69	0.794	0.801	−0.9	23.51	0.804	0.794	1.2	23.60	0.799	0.798	0.2
Sep	21.53	0.712	0.725	−1.9	20.36	0.679	0.684	−0.8	20.95	0.695	0.705	−1.4
Oct	15.94	0.519	0.530	−2.2	15.48	0.496	0.514	−3.7	15.71	0.507	0.522	−3.0
Nov	12.94	0.433	0.426	1.7	11.39	0.381	0.371	2.5	12.17	0.407	0.398	2.1
Dec	11.28	0.359	0.368	−2.4	9.81	0.316	0.316	0.0	10.55	0.338	0.342	−1.2
Mean	**19.29**	**0.658**	**0.647**	1.06	**19.01**	**0.649**	**0.637**	1.27	**19.15**	**0.653**	**0.642**	1.16

3.3 Impact of urbanization on G and UV radiation values received at Cairo urban area

Urbanization and industrialization processes have increased very rapidly in and around Cairo city. These processes cause not only an increase of atmospheric pollutants, which are harmful to human health and comfort, but also create several serious environmental problems. One of these problems is the attenuation of solar radiation components received at the Earth's surface especially the ultraviolet radiation. In order to investigate the effect of urbanization processes on the total global and ultraviolet solar radiation received at the urban area of Cairo, the monthly mean values of G and UV radiation for the old period (1969–1973) have been compared with the corresponding values of the recent period (1993–1997). The above two equal periods were selected for this study, because the measurements of G and UV radiation began at Cairo in 1969 and 1990, respectively. Furthermore, the monthly mean values of the total column ozone (O_3) retrieved from DOBSON surface observations at Cairo for the above two periods are also compared and taken into consideration to avoid the defects of neglecting effect of

127

stratospheric ozone on the modification of G and UV radiation values. The values of the old period (1969–1973) have been taken as reference base values for the non-urbanized period, while the values of the recent period (1993–1997) have also been taken to represent the heavy urbanized period. The used data of G, UV radiation, and O_3 have been obtained from the Egyptian Meteorological Authority, except UV radiation values for the non-urbanized period (1969–1973), where there are no measured values for UV radiation. Therefore, the monthly mean values of UV radiation have been estimated for the period (1969–1973) using the corresponding values of G for the same period and applying the deduced empirical formula (Eq. (2)). Furthermore, the monthly mean values of the percentage reduction (E%) of G, UV radiation, and O_3 values have been calculated for the recent urbanized period. The results and used data are presented and illustrated by *Figs. 2–5*. Also, the seasonal mean values of the G, UV radiation, and O_3 have been calculated for both non-urbanized and urbanized periods, and the results are given in *Table 2* with their percentage reductions.

Table 2. The seasonal mean values of G, UV radiation (MJ m^{-2}), and O_3 (DU) at Cairo urban area during the two periods (1969–1973 and 1993–1997), as well as the relative percentage reduction of their values, E%

Season	G			UV			O_3		
	1969–1973	1993–1997	E%	1969–1973	1993–1997	E%	1969–1973	1993–1997	E%
Winter	14.83	11.14	24.9	0.492	0.313	36.3	298	294	1.2
Spring	24.38	21.00	13.9	0.825	0.625	24.2	316	307	2.8
Summer	28.63	24.84	13.2	0.973	0.779	19.9	297	294	0.9
Autumn	19.13	15.86	17.1	0.642	0.463	27.8	283	275	2.6
Annual mean	**21.74**	**18.21**	**17.3**	**0.733**	**0.545**	**27.1**	**298**	**293**	**1.9**

A high variability of G and UV radiation values from month to month can be clearly seen in *Figs. 2* and *3*. This variability is caused not only by cloudiness but also the changing aerosol load. The monthly mean values of both G and UV radiation rise very regularly from a minimum value in December to a maximum value in July in both periods (1969–1973 and 1993–1997). Furthermore, during the non-urbanized period (1969–1973), the maximum values of G and UV radiation were 29.32 and 0.997 MJ m^{-2} and the minimum values were 13.35 and 0.440 MJ m^{-2}, respectively, while in the recent urbanized period (1993–1997), the maximum values of G and UV

radiation were 26.09 and 0.820 MJ m^{-2} and the minimum values were 9.95 and 0.268 MJ m^{-2}, respectively (*Figs. 2* and *3*). It could be also noticed, that the radiation values of the non-urbanized period are always higher than the values found in the recent urbanized period throughout the months of the year. The annual mean values of G and UV radiation (21.83 and 0.736 MJ m^{-2} for G and UV, respectively) during the non-urbanized period have been found higher than those of the urbanized period (18.21 and 0.548 MJ m^{-2} for G and UV, respectively) (*Table 2*). This is ascribed to the serious combined effects of the recently increased atmospheric pollution as sequence of increasing population, urbanization, and industrialization, as well as stationary and mobile sources of combustion in and around Cairo city.
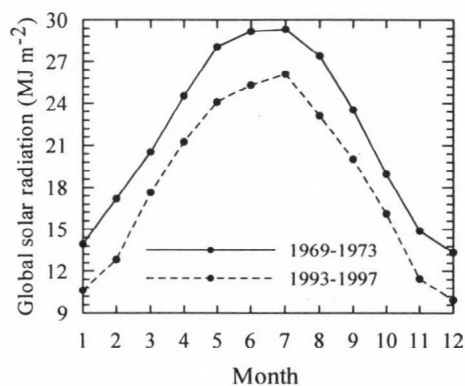
Fig. 2. The monthly variation of G radiation during the non-urbanized period (1969–1973) and urbanized period (1993–1997) at Cairo urban area.
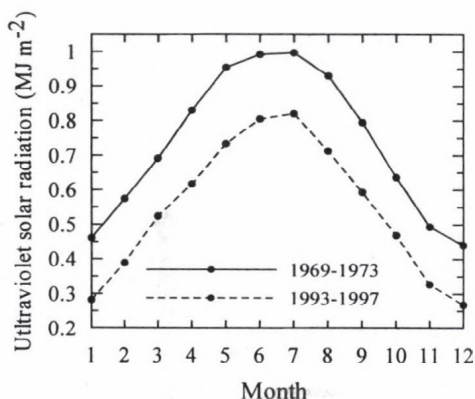
Fig. 3. Same as Fig. 2, but for UV radiation.

On the other hand, in *Fig. 5* and *Table 2*, the relative percentage reduction (E%) of both G and UV radiation at the urban area, induced by recent urbanization processes, varies from month to month and from season to season. The heavy maximum reduction of the two radiation components occurred in December (winter season) (E=25.5% and 39.1% for G and UV, respectively), while the minimum reduction occurred in July (summer season) (E=11.0% and 17.8% for G and UV, respectively). This is due to the fact, that the winter season has recently higher levels of aerosol and atmospheric pollutants than the summer season. This result agrees with the findings of *Robaa* (1999), who found that the pollutant and aerosol concentrations, liberated recently from urbanization and industrialization processes, have been increased for more than threefold in the winter season and around double in

the summer season. The annual mean relative reduction of G and UV were 17.4% and 27.4%, respectively. It is also clearly noticed, that the UV radiation is more attenuated than the G radiation during all months of the year (*Fig. 5*). This is due to the fact that radiation loss due to pollutant aerosols is strongly wavelength-dependant, and the shorter wavelengths are much more seriously affected than the longer wavelengths. This means that the UV component of solar radiation is subjected to the greatest atmospheric scattering obeying the well-known Rayleigh scattering process (*Rizk et al.*, 1985; *Sami and Al-Aruri*, 1990).

On the other hand, it can be seen that the annual variation of the values of stratospheric ozone, O_3, are irregular at Cairo, and the values of non-urbanized period (1969–1973) are always higher than the values found in the recent urbanized period (1993–1997), throughout the year months (*Fig. 4*). This is due to effect of the released pollutant gases, which increase the content of chlorine in the stratosphere with a consequent depletion of ozone (*Watson*, 1988). Furthermore, it was found that O_3 attained its maximum value (316 and 307 DU for non-urbanized and urbanized periods, respectively) in the spring season, mainly March, while the minimum value (283 and 275 DU for non-urbanized and urbanized periods, respectively) occurred in the autumn season, mainly in October and November.
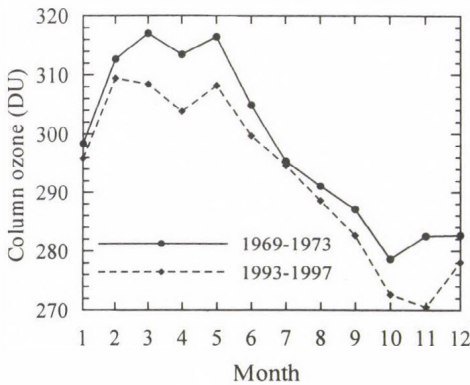
Fig. 4. Same as Fig. 2, but for ozone amount.
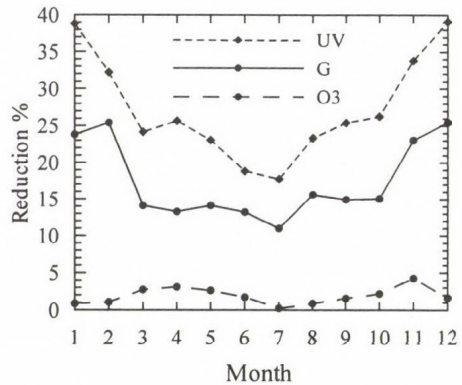
Fig. 5. Monthly variation of the calculated percentage reduction of G, UV, and O_3 during the urbanized period (1993–1997).

It is also noticed, that the ozone values have been weakly attenuated during the recent urbanized period (*Figs. 4* and *5* and *Table 2*). The monthly mean values of the reduction of O_3 are also irregular and ranged between –0.25% in July to 4.25% in November, while the annual mean value was 1.89%. This result agrees with the finding of *Shaltout et al.* (1994) and *Salem* (2000), who

found that the stratospheric ozone is stable and has normal density over Cairo City. Although the attenuation in the stratospheric ozone at any place causes increase of UV radiation values, the reverse process occurred at Cairo urban area and the UV radiation values are attenuated. This has two reasons: first, as motioned above, the percentage values of ozone attenuation are small. Second, the increased UV values, as a result of the attenuation in ozone amounts, could be lost by the significant effects of urbanization processes. Therefore, it could be concluded, that the urbanization and industrialization processes are considered the distinct main reason in the reduction of the solar radiation component values at the urban area of Cairo.

3.4 Comparative studies on G and UV radiation at rural and urban areas

Five years mean G and UV solar radiation data (1993–1997) for both urban (Cairo) and rural (Bahtim) areas are presented and compared. The used G and UV radiation data have been obtained from the Egyptian Meteorological Authority, except UV radiation values at the rural area of Bahtim, where there are no measurements for UV radiation. Therefore, for the comparative purposes, the values of UV radiation have been estimated using the corresponding values of G radiation and applying the deduced empirical formula (Eq. (2)). The monthly mean values of the urban-rural percentage reduction (E%) for G and UV radiation have also been calculated. The results and used data are presented and illustrated by *Figs. 6–8*.

In *Figs. 6* and *7*, it was found that both urban and rural areas have similar annual variation of G and UV radiation with higher values at rural area throughout the months of the year. This is attributed to an urban area, which is characterized by highly polluted air and fine particulate grains. Consequently, a loss in the energy of solar beam received by the surface due to backscattering and absorption, while high radiation values over the rural area is attributed to its rural site dominated by vegetation and characterized by clearness of its atmosphere. The values of G radiation at the rural area ranged between 10.72 MJ m^{-2} in December and 27.74 MJ m^{-2} in June, while UV radiation ranged between 0.348 MJ m^{-2} in December and 0.942 MJ m^{-2} in June.

It could be noticed, that the urban-rural global and ultraviolet reduction values vary from month to month according to the exchanged effects of cloud cover and air pollution intensities induced by urbanization processes. E% values ranged between 3.3% and 9.0% for G radiation and between 10.4% and 23.0% for UV radiation (*Fig. 8*). Generally, the urban area receives 7.0% less G and 17.8% less UV radiation compared to rural area, as annual average. This result agrees with finding of *Galindo* (1962), who found that the global radiation attenuation is 10% for Mexico city compared to rural surroundings,

and *Padmanabhamurty* and *Mandal* (1981), who also found significant urban and rural radiation differences for Delhi city. In our study, the relatively lower G radiation attenuation for urban area (Cairo) compared to rural surrounding (Bahtim) is perhaps due to the effect of surface wind, which causes rapid transportation of pollutants from the urban complex to neighboring rural area.
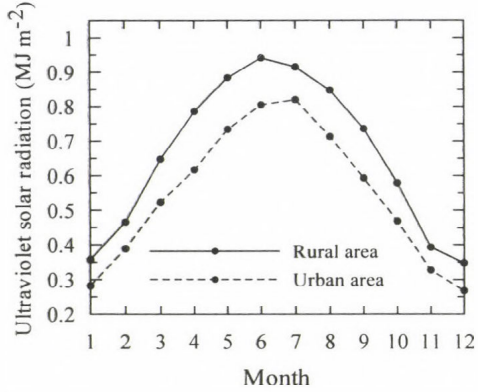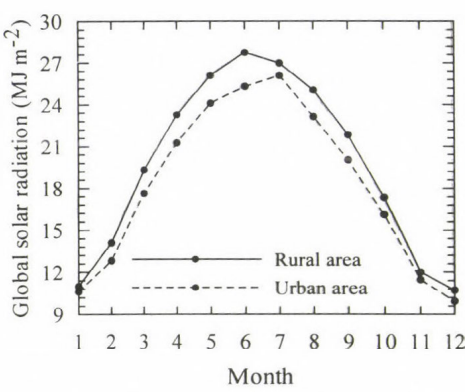
Fig. 6. Monthly variation of G radiation at both urban (Cairo) and rural (Bahtim) areas during the urbanized period (1993–1997).

Fig. 7. Same as Fig. 6, but for UV radiation.
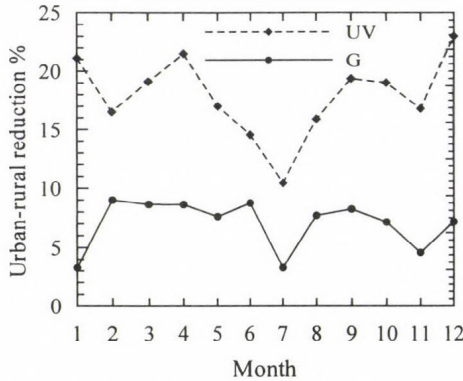
Fig. 8. Monthly variation of the calculated urban-rural percentage reduction of G and UV radiation during the urbanized period (1993–1997).

In *Fig. 8*, one can notice that the monthly mean percent reduction in the received UV radiation is higher than in G radiation in the urban area of Cairo. This is due to the UV component of solar radiation, which is a subject to the greatest atmospheric scattering obeying, the well-known Rayleigh scattering process (*Sami* and *Al-Aruri*, 1990). A large drop in the reduction of urban-

rural global and ultraviolet radiation is well noticed in July (*Fig. 8*). The reason of this drop is that the summer season (mainly July) is characterized by cloudless skies and lower levels of aerosol and atmospheric pollutants (*Robaa*, 1999).

3.5 Seasonal variation of the ratio UV/G

Fig. 9 shows the monthly variation of the ratio UV/G for Cairo during the non-urbanized (1969–1973) and urbanized periods (1993–1997) compared with UV/G values of two sites in the Arabian peninsula: Kuwait city in Kuwait (*Al-Aruri et al.* 1988) and Makkah in Saudi Arabia (*Khogali* and *Al-Bar*, 1992).
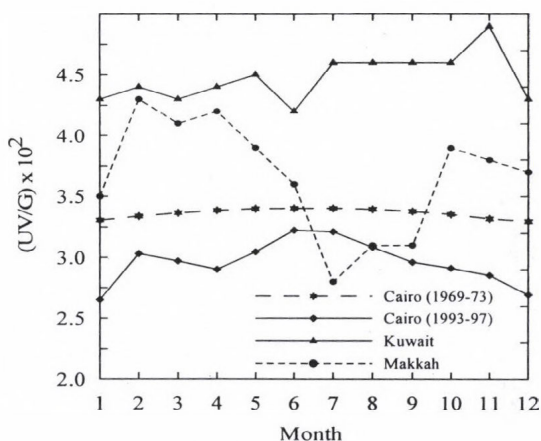
Fig. 9. Monthly variation of UV/G ratio for Cairo during the two periods (1969–1973 and 1993–1997) compared with UV/G for Kuwait and Makkah.

From this figure we can deduce the following:

- At all sites the ratio UV/G ranged between 2.7% and 4.9%.
- The lower values of UV/G occurring in winter are caused by lower solar elevation during this season.
- Cairo ratio of the urbanized period (1993–1997) is the lowest value compared to all other sites most of the year. This is due to the high air pollution in Cairo city produced by traffic and industrial activities. The curve of the non-urbanized period (1969–1973) has higher values than those of the urbanized period (1993–1997), and characterized by a very slight seasonal variation. This may be caused by the fact that the attenuation of UV that occurs during the recent period (1993–1997) is

higher than the attenuation of G as shown in *Fig. 8*, while the higher ratios UV/G during the non-urbanized period can be explained by the stronger absorption of G, that has longer wavelength than UV, due to the water vapor droplets of cloud. Similar features were also observed at Potsdam by *Fiester* and *Grasnick* (1992).

- Kuwait ratio is the highest compared to all other sites most of the year. It is possibly due to the effect of Iraq-Iran war during the 1980's on the stratosphere over Kuwait, where G and UV radiation measurements in Kuwait is performed from July 1985 to June 1987 during the war (*Al-Aruri et al.* 1988).

- Makkah ratio has relatively higher values most of the year. This is due to the population (over one million people) and transporting vehicles gathered in July and August in the pilgrimage season of 1987. A large drop in the ratio UV/G is also observed in Makkah from July to September. This may be because of the attenuation of UV by dust and low tropospheric ozone during these months (*Khogali* and *Al-Bar*, 1992).

- The values of UV/G are higher for Kuwait and Makkah than for Cairo due to the stronger absorption of G and weaker absorption of UV at these two sites. This may be due to the difference in size and amount of the fine particles at both Kuwait and Makkah, or disturbances in the ozone layer at Kuwait due to Gulf war, or both (*El-Hadidy et al.* 1990).

3.6 The effect of atmospheric aerosols on G and UV solar radiation at Cairo

To study the effect of atmospheric aerosols on both G and UV solar radiation at Cairo, we selected the dusty days of the five years period from 1990 to 1994 for the urban area of Cairo, and only five days were available. The mentioned period (1990–1994) was selected for availing this data. During the same period, an equal number of dust free days were chosen. The chosen dust free days were in the same year and month that the dusty ones. It is of value to note here, that the dusty days were chosen with visibility less than 10 km, while dust free days had a visibility of more than 20 km. It must be noted that: (a) the technique, by which we selected clear days, is a draft method using horizontally measured visibility, and thus gives approximative estimation, (b) the ozone content is not considered for the above calculations and the quantitative establishments are valid solely for the days used, thus the percentage values cannot be considered characteristic or normal values. Under this choice, percentage of reduction in the received G and UV components were calculated and listed in *Table 3*. It was found, that the reduction in the received G and UV radiation due to the effects of the aerosol particles ranged between 26% and 45% for G and between 33% and 59% for UV. One can

134

also notice, that the maximum percentage reduction in the received G (45%) and UV (59%) radiation is higher than such reduction in the G and UV radiation induced by urbanization processes at Cairo (*Table 3*). This is due to the simultaneous combined effects of aerosol particles, urbanization, and industrialization processes during the dusty days.

Table 3. Calculated percentage reduction in the received total daily G and UV solar radiation due to the effect of atmospheric aerosols at the urban area of Cairo

Days	Reduction (%)	
	G	UV
March 05, 1990** March 22, 1990*	43	58
March 18, 1991** March 05, 1991*	26	33
April 22, 1992** April 15, 1992*	32	47
May 10, 1993** May 25,1993*	45	59
April 03, 1994** April 17, 1994*	38	46

* Clear day   ** Dusty day

One can also notice, that the percentage reduction in the received UV radiation is always higher than such reduction in G radiation during all dusty days (*Table 3*). This result can be attributed to, as mentioned before, the absorption by solid particles and to the known Rayleigh scattering, which varies with the inverse fourth power of the wavelength (λ^{-4}). Consequently, the UV component of solar radiation is a subject to the greatest atmospheric scattering. These results agree with the findings of both *Sami* and *Al-Aruri* (1990) and *Salem* (2000).

3. Conclusions

Although the study of ultraviolet, UV, solar radiation is very important because of its dramatic biological effects on humans, animals, plants, the earth's surface, and the surrounding atmosphere, the concerned studies of UV radiation is very rare in Egypt. Therefore, the present study is an attempt to study the characteristics and behavior of UV beside the total global, G,

radiation and the impact of urbanization on their received values at Cairo urban area. The measured and estimated values of G and UV radiation beside stratospheric ozone, O_3, over urban (Cairo) and rural (Bahtim) areas during a non-urbanized (1969–1973) and urbanized period (1993–1997) have been used. Also, the effect of atmospheric dust on G and UV radiation is also investigated and discussed. The results could be summarized in the following:

- A significant correlation between G and UV radiation has been found with correlation coefficient 0.98 and the standard error was close to zero. The recommended correlation equation has been stated to estimate the values of UV radiation which is difficult to measure at any site in the zone of Lower Egypt.

- The monthly mean values of G and UV received at Cairo urban area during the non-urbanized period highly exceeds the values received during the urbanized period for all months of the year.

- At Cairo urban area, the annual mean values of G and UV radiation were 21.83 and 0.736 MJ m^{-2} during the non-urbanized period and 18.21 and 0.548 MJ m^{-2} during the urbanized period, while the mean relative reduction of G and UV were 17.4% and 27.4%, respectively. The UV radiation is more attenuated than G radiation during all months of the year. This is due to the radiation loss caused by pollutant aerosols, which is strongly wavelength-dependant, and the shorter wavelengths are much more seriously affected than longer wavelengths.

- The increase in UV values, as a result of the attenuation in ozone amount at Cairo, was lost by the significant effects of urbanization processes, that reduce the solar radiation amounts. Therefore, it could be concluded, that the urbanization and industrialization processes are considered the distinct main reason in the reduction of the values of the solar radiation components at Cairo urban area.

- A comparative study for G and UV radiation at both urban and rural areas during the urbanized period (1993–1997) revealed, that the urban area always has values of G and UV radiation distinctly lower than that found in rural area for all months of the year. Urban-rural mean reduction of G and UV were 7.0% and 17.9%, respectively.

- The ratio UV/G of the non-urbanized period (1969–1973) has higher values than those of the urbanized period (1993–1997), and characterized by very slight seasonal variation caused by the attenuation of UV. The attenuation of UV in the urbanized period is higher than that of G, while the higher values of the non-urbanized period can be explained by the stronger absorption of G, that has longer wavelength than UV, due to the water vapor droplets of cloud.

- In the dusty days, the reduction in the received G and UV radiation due to the effects of atmospheric aerosol particles ranged between 26% and 45% for G and between 33% and 59% for UV. The maximum percent reduction in the received G (45%) and UV (59%) radiation was higher than the same reduction in the G and UV radiation induced by urbanization processes at Cairo. This is due to the simultaneous combined effects of aerosol particles and urbanization processes during the dusty days. The quantitative establishments are valid solely for the days used, and the percentage values cannot be considered characteristic or normal values.

References

Al-Aruri, S., Rasas, M., Al-Jamal, K., and *Shaban, N.,* 1988: An assessment of global ultraviolet radiation in the range (0.290-385 μm) in Kuwait. *Sol. Energy 41,*159-162.

Biswas, A.K., 1979: *The Ozone Layer.* Vol. 4. Pergamon Press, Oxford.

El-Hadidy, M.A., Abdel-Nabi, D.Y., and *Kruss P.D.,* 1990: Ultraviolet solar radiation at Dhahran, Saudi Arabia. *Sol. Energy 44,,* 315-319.

Fiester, U. and *Grasnick, K.H.,* 1992: Solar UV radiation measurements at Potsdam (52°22'N; 31°5'E). *Sol. Energy 49,* 541-548.

Galindo, I., 1962: La radiacion en Mexico en 1957 (Global radiation in Mexico city). Instituto de Geafisica, UNAM.

Giese, A.C., 1982: Living with our Suns' Ultraviolet Rays. Plenum Press, New York.

Khogali, A. and *Al-Bar, O.F.,* 1992: A study of solar ultraviolet radiation at Makkah solar Station. *Sol. Energy 48,* 79-87.

Kirchhoff, V.W., Silva, A., and *Pinheiro, K.,* 2002: Wavelength dependence of aerosol optical thickness in the UV-B band. *Geophys. Res. Lett. 29,* 1620, doi:10.1029/2001.

Koronakis, P.S., Sfantos, G.K., Paliatsos, A.G., Kaldellis, J.K., Farofalakis J.E., and *Koronaki, I.P.,* 2002: Interrelations of UV-global/global/diffuse solar irradiance components and UV-global attenuation on air pollution episode days in Athens, Greece. *Atmos. Environ. 36,* 3173-3181.

Kylling, A., Dahlback, A., and *Mayer, B.,* 2000: The effect of clouds and surface albedo on UV irradiances at a high latitude site. *Geophys. Res. Lett. 27,* 1411-1414.

Luccini, E., Cede, A., and *Piacentini, R.D.,* 2003: Effect of clouds on UV and total irradiance at Paradise Bay, Antarctic Peninsula, from a summer 2000 campaign. *Theor. Appl. Climatol. 75,*105-116.

McKenzie, R.L., Blumthaler M., Booth C.R., Diaz S.B., Frederick J.E., Ito T., Madronich S., and *Seckmeyer, G.,* 1995: Surface ultraviolet radiation. In Scientific Assessment of Ozone Depletion: 1994. *WMO Global Ozone Research and Monitoring Project Report,* No. 37, 9.1-9.22.

Padmanabhamurty, B. and *Mandal, B.B.,* 1981: Urban-rural radiation differences. *Mausam 33,* 509.

Parrish, J.A., Rox Arderson, R., Urbach, F., and *Pitts, D.,* 1978: *UV-A.* Plenum Press, New York.

Rizk, H.F., Farag, S.A., and *Ateia, A.A.,* 1985: Effect of pollutant aerosols on spectral atmospheric transmissivity in Cairo. *J. Environ. Int. 11,* 487-492.

Robaa, S.A., 1999: Impact of urbanization on meteorology and human comfort in Greater Cairo, Egypt. *Ph.D. Thesis.* Astronomy and Meteorology Dept., Faculty of Science, Cairo University.

Salem, A.I., 2000: Analysis and correlation of ultraviolet solar radiation from routine meteorological measurements over Egypt. *Mausam 51*, 275-280.

Sami, D. and *Al-Aruri*, 1990: The empirical relationship between global radiation and global ultraviolet (0.290-0.385 μm) solar radiation components. *Sol. Energy 45*, 61-64.

Shaltout, M.A., Ghonim, M.M., Trabea, A.A., and *Allam, H.*, 1994: Ultraviolet solar radiation over Egypt. *World Renewable Energy Congress – III*. Reading University, U.K., 5, 2, 1506-1509.

Som, A.K., 1992: Solar UV-B radiation measurements over Bahrain. Renew. Energ 2, 93-98.

Tnag, X., Madronich, S., Wallington, T., and *Calamari, D.*, 1998: Changes in tropospheric composition and air quality. *J. Photoch. Photobio. B 46*, 83-95.

Watson, R.T., 1988: Present state of knowledge of the upper atmosphere. *An assessment report. NASA RP-1208*, Washington D.C.

Wuttke, S., Verdebout, J., and *Seckmeyer, G.*, 2003: An improved algorithm for satellite derived UV Radiation. *Photochem. Photobiol. 77*, 52-57.

Zerefos, C.S., Balis, D., Tzortziou, M., Bais, A., Tourpali, K., Meleti, C., Bernhard, G., and *Herman, J.*, 2001: A note on the interannual variation of UV-B erythemal doses and solar irradiance from ground – based and satellite observations. *Ann. Geophys. 19*, 115-120.

BOOK REVIEW

András Gelencsér: **Carbonaceous Aerosol**. Springer, 2004, Dordrecht, The Netherlands, 350 pages, with a rich reference list, and several figures and tables.

Hungarian aerosol research started about forty-five years ago. The original aim was to determine the nature of atmospheric aerosol particles serving as condensation nuclei during cloud formation. For this reason great efforts were devoted to identify water-soluble substances and the size distribution of particles consisting of these materials. At that time this obviously meant *inorganic ions*. This was due to the fact that practically nobody believed that organic compounds existing in the aerosol also contains water-soluble species. Secondly, analytical methods for detecting such materials were rather scanty. Organic compounds in the particles were investigated solely in air pollution studies after dissolving the aerosol samples in organic solvents. However, these studies clearly showed that species analyzed give only a small fraction of the total mass of organic substances. Since the natural solvent in atmospheric environment is water, it became clear that the study of possible water-soluble *organic species* is obviously needed if we want to understand cloud and precipitation formation in the atmosphere.

Such research began ten years ago at the University of Veszprém, partly in European cooperation, by the workers of the Air Chemistry Group sponsored by the Hungarian Academy of Sciences. Their efforts have given important results in the field outlined. At the same time a new generation of young scientists with background in chemistry was formed, who are able to do this complicated research. In this respect the author of this book is a good example. As the chapters show, he and his associates not only have made an excellent research, but also his knowledge gained made it possible to write the first book on carbonaceous aerosol.

The volume consists of five chapters. After the first introductory part, the sampling and analytical techniques making the observation of carbonaceous particles of different types in the air possible are summarized. The third chapter is devoted to the presentation of major carbonaceous particle types and their sources. The classification of carbon containing species (excluding carbonates of negligible significance) is not an easy task. Except soot particles of various types (black carbon, elemental carbon), a major part of carbonaceous materials is composed of organic matter of different kind and nature. The organic particles can be directly emitted into the air by natural

sources (vegetation, living organism, soil and oceans) as well as by human activity. The latter includes biomass and fossil fuel burning. The total global release of these primary particles is around 10 Tg yr^{-1} expressed in carbon equivalents. At least the same amount of organic particulate mass (secondary organic particles) is produced yearly by chemical reactions and condensation in the air of organic gases and vapors liberated by biogenic and anthropogenic processes. The study of secondary organic particle formation is rather difficult. It seems, however, that ozone and hydroxyl radicals play an important part in the control of the oxidation of organic precursor gases, which leads to condensable species. The estimation of the partition of gaseous and aerosol phases also an essential, but not well-solved problem. Although the formation of organic compounds with relatively low carbon number is possible in this way, the production of humic-like substances (HULIS), composed of macromolecules, is determining in particular. This is due to the observational fact indicating that the concentration of this group of compounds is very substantial in the air, and a part of them is soluble in water. It is to be noted that the author of this volume, and the group in Veszprém, carried out important work concerning this new subject.

The fourth chapter is entitled "Organic chemistry of aerosol". In this chapter the chemical and physical properties of organic aerosol are summarized, including such essential properties as the concentration, size distribution, and scavenging by cloud and rain of organic particles. The possibility of using organic particles as tracers is also outlined. From meteorological point of view, the last chapter is particularly interesting. The reader understands from this chapter: why the study of organic particles is so important. Thus, the optical properties of organic aerosol are presented and discussed from the point of view of radiation transfer in the atmosphere. Further, the hygroscopic behavior of particulate organic species is also described. Their possible effects on condensation and ice nucleation are explained in a very convincing manner. Since the organic particles influence the cloud structure, it is evident that they play an important part not only in the control of water cycle, but also in the indirect aerosol climatic forcing. Finally, a subchapter deals with the role of carbonaceous particles in the heterogeneous reaction in the atmosphere.

In summary we can conclude that *Gelencsér* wrote a very precious book. First, it gives an excellent review of a new branch of atmospheric aerosol chemistry. Secondly, the volume indicates the development of atmospheric chemistry. It makes it obvious that professional chemists can make an important contribution to the evolution of atmospheric science. The last chapter also proves that such chemical studies are very useful to a deeper understanding of such classical meteorological problems as cloud and

precipitation formation, solar and terrestrial radiation transfer, and climate in general.

The volume, published in the Atmospheric and Oceanographic Science series of the editor, is thus proposed to everybody, for example meteorologists and chemists, interested in up-to-date art of state of the science of atmospheric environment.

E. Mészáros

Wilford Zdunkowski and *Andreas Bott:* **Dynamics of the Atmosphere. A Course in Theoretical Meteorology.** Cambridge University Press, Cambridge, 2003. 719 pages, 187 figures.

Wilford Zdunkowski and *Andreas Bott*: **Thermodynamics of the Atmosphere. A Course in Theoretical Meteorology.** Cambridge University Press, Cambridge, 2004. 251 pages, 37 figures.

There are many "classical" schools of theoretical meteorology, one of them is the German School. There were many highlights of the activity of German meteorologists in the last one and a half centuries, and the influence generated by the meteorological reference books and university textbooks of the German School is very strongly perceptible in the meteorological communities of the Central and Eastern European countries.

Wilford Zdunkowski, retired professor of the Johannes Gutenberg University in Mainz and *Andreas Bott*, professor of the Rheinische Friedrich Wilhelms University in Bonn, former lecturer of the Mainz University have declared in the preface to their book to be determined by the activity of legendary predeccesors like professors *K. H. Hinkelmann* and *J. G. Korb*.

The structure and way, the various topics of the dynamics and thermodynamics of the atmosphere are discussed, are similar to the methods of the German School.

The dynamics of the atmosphere is discussed in two independent parts in one book. It is quite common in university textbooks of dynamic meteorology to treat basic mathematics in the introductory chapters, but it is novel to divide the book into two independent parts: one dealing with pure mathematics and one with applied mathematics, i.e., the dynamics of the atmosphere. The most important mathematical tools of vector algebra, vector function theory, differential and integral calculus are peresented in Part I. Even the concept of nonlinear dynamics is discussed here.

Part II of this heavy textbook gives all the basic elements of dynamic meteorology in 27 chapters. Such rarities like the usage of the natural coordinate system can also be found in the book. A detailed and profound discussion of atmospheric wave motions, especially Rossby wave motions, are given by the authors. The description of boundary layer processes is also a valuable part of the book. The chapters dealing with the role of baroclinic instability, atmospheric modeling, and predictability summarize the results of theoretical meteorology of the last couple of decades.

The coursebook on thermodynamics gives a broad spectrum of the knowledge of physical thermodynamics applied to atmospheric processes. After the basic concepts the fundamental laws of thermodynamics are discussed. Thermodynamic potentials and stability conditions, thermodynamic diagrams and special adiabats are presented in full details. Chapters presenting thermal radiation, constitutive equations for irreversible fluxes, and state functions for cloud air are further substantial parts of the book.

Sets of exercises (160 in the first and 80 in the second volume) make the books profitable both for undergraduate and graduate students of meteorology.

Hungarian readers of the volumes, who are familiar with the footprints of the classical German meteorological school in the traditional textbooks of *Frigyes Dési, Ferenc Rákóczi,* and *Gusztáv Götz,* will most probably welcome the new results of the last quarter of a century on the dynamics and thermodynamics of the atmosphere, worked into these fine volumes.

Gy. Gyuró

GUIDE FOR AUTHORS OF *IDŐJÁRÁS*

The purpose of the journal is to publish papers in any field of meteorology and atmosphere related scientific areas. These may be

- research papers on new results of scientific investigations,
- critical review articles summarizing the current state of art of a certain topic,
- short contributions dealing with a particular question.

Some issues contain "News" and "Book review", therefore, such contributions are also welcome. The papers must be in American English and should be checked by a native speaker if necessary.

Authors are requested to send their manuscripts to

Editor-in Chief of IDŐJÁRÁS
P.O. Box 39, H-1675 Budapest, Hungary

in three identical printed copies including all illustrations. Papers will then be reviewed normally by two independent referees, who remain unidentified for the author(s). The Editor-in-Chief will inform the author(s) whether or not the paper is acceptable for publication, and what modifications, if any, are necessary.

Please, follow the order given below when typing manuscripts.

Title part: should consist of the title, the name(s) of the author(s), their affiliation(s) including full postal and E-mail address(es). In case of more than one author, the corresponding author must be identified.

Abstract: should contain the purpose, the applied data and methods as well as the basic conclusion(s) of the paper.

Key-words: must be included (from 5 to 10) to help to classify the topic.

Text: has to be typed in double spacing with wide margins on one side of an A4 size white paper. Use of S.I. units are expected, and the use of negative exponent is preferred to fractional sign. Mathematical formulae are expected to be as simple as possible and numbered in parentheses at the right margin.

All publications cited in the text should be presented in a *list of references*, arranged in alphabetical order. For an article: name(s) of author(s) in Italics, year, title of article, name of journal, volume, number (the latter two in Italics) and pages. E.g., *Nathan, K.K.,* 1986: A note on the relationship between photo-synthetically active radiation and cloud amount. *Időjárás 90,* 10-13. For a book: name(s) of author(s), year, title of the book (all in Italics except the year), publisher and place of publication. E.g., *Junge, C. E.,* 1963: *Air Chemistry and Radioactivity.* Academic Press, New York and London. Reference in the text should contain the name(s) of the author(s) in Italics and year of publication. E.g., in the case of one author: *Miller* (1989); in the case of two authors: *Gamov* and *Cleveland* (1973); and if there are more than two authors: *Smith et al.* (1990). If the name of the author cannot be fitted into the text: *(Miller,* 1989); etc. When referring papers published in the same year by the same author, letters a, b, c, etc. should follow the year of publication.

Tables should be marked by Arabic numbers and printed in separate sheets with their numbers and legends given below them. Avoid too lengthy or complicated tables, or tables duplicating results given in other form in the manuscript (e.g., graphs)

Figures should also be marked with Arabic numbers and printed in black and white in camera-ready form in separate sheets with their numbers and captions given below them. Good quality laser printings are preferred.

The text should be submitted both in manuscript and in electronic form, the latter on diskette or in E-mail. Use standard 3.5" MS-DOS formatted diskette or CD for this purpose. MS Word format is preferred.

Reprints: authors receive 30 reprints free of charge. Additional reprints may be ordered at the authors' expense when sending back the proofs to the Editorial Office.

More information for authors is available: antal.e@met.hu

Information on the last issues: http://omsz.met.hu/irodalom/firat_ido/ido_hu.html